Recurrent wavelet neural network control of a PMSG system based on a PMSM wind turbine emulator

Chih-Hong LIN∗

Department of Electrical Engineering, National United University, Miaoli, Taiwan

Abstract: A recurrent wavelet neural network (NN)-controlled 3-phase permanent magnet synchronous generator system (PMSG), which is direct-driven by a permanent magnet synchronous motor (PMSM) based on a wind turbine emulator, is proposed to control the output values of a rectifier (or AC to DC power converter) and inverter (or DC to AC power converter) in this study. First, a closed-loop PMSM drive control based on a wind turbine emulator is designed to generate the maximum power for the PM synchronous generator (PMSG) system according to different wind speeds. Next, the rotor speed of the PMSG, the DC bus voltage, and the current of the power converter are detected simultaneously to yield a better power output of the converter through DC bus power control. Because the PMSG system is a nonlinear and time-varying dynamic system, one online-trained recurrent wavelet NN controller is developed for the tracking controller of the DC bus power to improve the control performance in the output end of the rectifier. Additionally, another online-trained recurrent wavelet NN controller is also developed for tracking the controller of the AC power to improve the control performance in the output end of the inverter. Finally, some experimental results are verified to show the effectiveness of the proposed recurrent wavelet NN-controlled PMSG system direct-driven by a PMSM based on a wind turbine emulator.

Key words: Permanent magnet synchronous motor, recurrent wavelet neural network, permanent magnet synchronous generator, rectifier, inverter

1. Introduction

Since petroleum is gradually being exhausted and the emphasis on environmental protection is progressively rising, the usage of clean energy sources such as wind, photovoltaics, and fuel cells has become very important and quite popular in electric power industries. Clean energy sources such as wind, photovoltaics, and fuel cells can be interfaced to a multilevel converter system for a high power application [1–3].

Wind turbines as a source of energy have progressively increased worldwide. Various control methods and conversion technologies for wind energy conversion systems are fast developing in energy conversion applications. The permanent magnet synchronous generator (PMSG) system has been used for wind power generating systems due to its many advantages, such as simpler structure, better reliability, lower maintenance, and higher efficiency [4–8]. Therefore, the PMSG system represents a significant trend in the progress of wind power applications [4–8]. The output power behavior of a wind turbine is nonlinear. The provided power of vertical-axis turbines is very sensitive to the load variation due to different structure effects [4–8]. Thus, control of the operating point is indispensable for the maximum output power. The controllable rectifier is used to convert the varied

---

AC voltage generated by the PMSG into a DC bus voltage. Next, the controllable inverter is used to convert the DC bus voltage into AC at a fixed frequency in order to provide for the stand-alone or grid applications of electrical utilizations. The major purposes of utilizing wind turbines are to extract the maximum power of the turbine and to deliver the appropriate energy to the stand-alone power or grid power system. According to these purposes, the better structure of the power conversion in wind turbines is the AC to DC to AC power converter [9,10].

Wavelet neural networks (NNs) [11–15] have been widely used for approximating arbitrary nonlinear functions [11–15], the identification of dynamic modeling [16–18] and control of nonlinear systems [19–22], and dynamic applications of various industries [23–27] due to the learning capability of NNs and the approximating capability of wavelet decomposition. In comparison with conventional NNs [28–31], the convergence of training algorithms for approximating arbitrary nonlinear functions in wavelet NNs has a lower number of iterations [32]. Since the structure of wavelet NNs can provide more capacity to abound the mapping relationship between the inputs and outputs, the wavelet NN has been proven to be better than the other NNs for the identification of nonlinear systems and the control of complex dynamical systems [32]. However, NNs, including wavelet NNs, are static input/output mapping schemes that can approximate a continuous function to an arbitrary degree of accuracy. Therefore, the recurrent NN [33–38] is based on supervised learning, which is a dynamic mapping network and is more suitable for describing dynamic systems than the NN. For this ability to temporarily store information, the structure of the network is simplified. The recurrent wavelet NN [39–43] combines the properties of the attractor dynamics of the recurrent NN and the good convergence performance of the wavelet NN. In [39–43], the recurrent wavelet NN dealt with time-varying inputs or outputs through its own natural temporal operation because of an input layer composed of internal feedback neurons to capture the dynamic response of a system.

Since PMSGs have a robust construction, lower initial cost, and lower maintenance cost, PMSGs are suitable for stand-alone or grid power sources in small wind energy applications. Therefore, a permanent magnet synchronous motor (PMSM) direct-drive PMSG system, using 2 sets of the same recurrent wavelet NN controllers as the adjusting controllers for both the DC bus voltage of the rectifier and the AC 60-Hz line voltage of the inverter, is introduced in this study. Two online-trained recurrent wavelet NNs are introduced as the adjusting controllers for both the DC bus voltage of the controllable rectifier and the AC 60-Hz line voltage of the controllable inverter. Moreover, the training algorithms of 2 sets of the same online-trained recurrent wavelet NNs based on backpropagation are derived to train the recurrent weights, connective weights, translations, and dilations. Additionally, for the comparison of the control performance, a proportional-integral (PI) controller can also be executed in the PMSG system. However, the control gains of the PI controller are obtained by the trial-and-error method, which is very time-consuming in practical applications. Because the PMSG system has many uncertainties, the adjusted capacity and tracking capacity of the output voltage as controlled using the PI controller is less improved. To raise the desired robustness and overcome the above problem, the recurrent wavelet NN controller is proposed to control the output DC bus voltage of the rectifier produced by the PMSM direct-drive PMSG system and control the output voltage of the inverter provided by the DC bus power. In the proposed recurrent wavelet NN controller, the recurrent weights, connective weights, translations, and dilations are trained online via a learning algorithm. Meanwhile, to demonstrate the better dynamic characteristics of the proposed controller, comparative studies with the PI controller and the conventional NN controller are demonstrated by experimental results. Therefore, the control performance of the proposed recurrent wavelet NN control is much improved and can be verified by some experimental results.

2. Description of the systems

The variable speed wind turbine of the PMSG system direct-driven by a PMSM is a complex electromechanical system, which includes the mechanical components, the PMSG, and so on. The description of these components is presented as follows.

2.1. Model of a wind turbine

The characteristic curve of the wind power versus the rotor speed for the model of a wind turbine at different wind speeds in the steady state, shown in Figure 1, is very important for a PMSG system direct-driven by a PMSM. The power specification of the adopted 3-blade horizontal axis-type wind turbine in this paper is 1.5 kW and its diameter is 2 m. It is capable of obtaining the working point of the wind turbine that uses the intersection point of the load characteristic curve and the turbine characteristic curve at a designated wind speed. It is a very important characteristic curve as the shaft power of the wind turbine relates to the wind speed v_1 and rotor speed ω_{r1} to the maximum power tracking, as seen in Figure 1. For convenient usage and application, the characteristic curve shown in Figure 2 can also be expressed as the characteristic curve of the wind turbine model. It represents the relationship curve between the coefficient $D_p(\beta)$ of the power performance and the tip speed ratio β. According to aerodynamic principles [1,4–7], the tip speed ratio β of the wind turbine can be represented as:
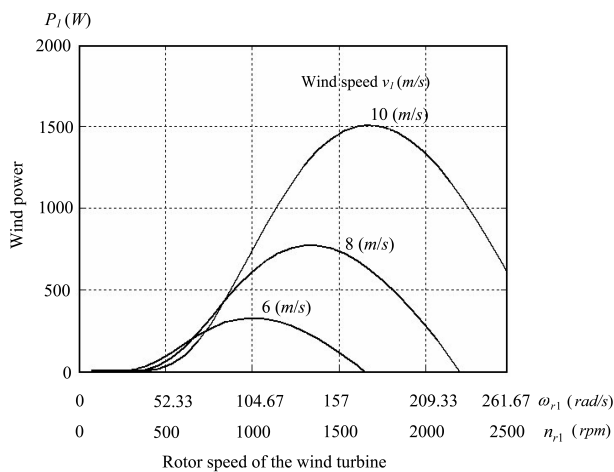

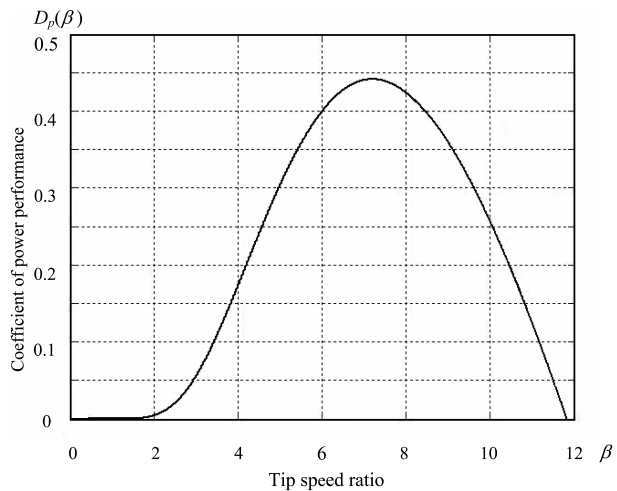**Figure 1.** Characteristic curves of wind power versus rotor speed for the wind turbine model at different wind speeds.

Figure 2. Characteristic curve of the coefficient $D_p(\beta)$ of power performance versus the tip ratio β for the wind turbine.

$$\beta = r_1\,\omega_{r1}/v_1, \tag{1}$$

where β is the tip speed ratio of the wind turbine, r_1 is the rotor radius of the wind turbine in meters, ω_{r1} is the rotor speed of the wind turbine in rad/s, and v_1 is the wind speed in m/s. The output mechanical power P_1 of the wind turbine can be expressed as [1,4–7]:

$$P_1 = \rho_1 A_1 D_p(\beta) v_1^3/2 = \rho_1 A_1 D_p(\beta) r_1^3 \omega_{r1}^3/(2\beta^3), \tag{2}$$

where ρ_1 is the density of the air in kg/m^3 and A_1 is the undraped area in m^2. The generated torque of the wind turbine for different wind speeds can be obtained from the $D_p(\beta) - \beta$ curve in the modeling usage. It

is very important that the aerodynamic efficiency is maximum at the optimum tip speed ratio. The produced torque of the wind turbine can be indicated as follows [1,4–7]:

$$T_1 = P_1/\omega_{r1} = \rho_1 A_1 D_p(\beta) v_1^3/(2\omega_{r1}) = \rho_1 A_1 R_1^3 D_p(\beta)\omega_{r1}^2/(2\beta^3), \qquad (3)$$

where T_1 is the produced torque of the wind turbine in Nm. The dynamic equation of the torque, which is the produced torque T_1 of the wind turbine subtracted by the electromagnetic torque T_{e1} of the PMSG, can be represented as:

$$T_1 - T_{e1} = J_1 \frac{d\omega_{r1}}{dt} + B_1\omega_{r1}, \qquad (4)$$

where J_1 is the moment of inertia of the PMSG and B_1 is the viscous friction coefficient of the PMSG.

2.2. Wind turbine emulator based on a PMSM

The wind turbine emulator that was proposed in [4–10] is adopted in this study in order to emulate the wind turbine. Additionally, the adopted field-oriented controlled PMSM can emulate the power speed characteristic curve of the wind turbine in this paper. In addition, a closed-loop robust speed controller, which can fight the intrinsic nonlinear and time-varying characteristic of the PMSM drive, is adopted to adjust the rotor speed with the relevant wind speed in order to emulate the wind variation.

2.3. Field-oriented controlled PMSG system

The voltage equations for the PMSG in the rotating reference frame can be indicated as follows [1,7–10]:

$$v_{q1} = -R_{s1}\, i_{q1} - L_{q1}\, \dot{i}_{q1} - P\omega_r L_{d1} i_{d1} + P\omega_{r1}\lambda_{pm}, \qquad (5)$$

$$v_{d1} = -R_{s1}\, i_{d1} - L_{d1}\, \dot{i}_{d1} + P\omega_{r1} L_{q1}\, i_{q1}, \qquad (6)$$

where v_{d1} is the $d-$axis stator voltage, v_{q1} is the $q-$axis stator voltage, i_{d1} is the $d-$axis stator current, i_{q1} is the $q-$axis stator current, L_{d1} is the $d-$axis stator inductance, L_{q1} is the $q-$axis stator inductance, R_{s1} is the stator resistance, and ω_{r1} is the rotor speed. A field-oriented control was adopted in [7–10]. Using the field-oriented control, the $d-$axis stator current can be set to 0; that is, $i_d = 0$. Moreover, the electromagnetic torque of the PMSG can be expressed as:

$$T_{e1} = \frac{3}{2}\frac{P}{2}\left[\lambda_{pm} i_{q1} - (L_{d1} - L_{q1}) i_{d1} i_{q1}\right] = \frac{3}{2}\frac{P}{2}\lambda_{pm} i_{q1} = K_t i_{q1}, \qquad (7)$$

where P is the number of poles, λ_{pm} is the permanent magnet flux linkage, and $K_t = 3P\lambda_{pm}/4$ is the torque constant. For convenient analysis, the field-oriented controlled PMSG system is adopted. To emulate the operation of the wind turbine, the primary machine's PMSM is directly mounted to the PMSG. The control principle of the PMSG system is based on field orientation. Due to $L_{d1} = L_{q1}$ and $i_{d1} = 0$ in the PMSG system, the second term of Eq. (7) is 0. Moreover, λ_{pm} is constant for the field orientation control of the PMSG system. The electromagnetic torque T_{e1} is a function of i_{q1}. The electromagnetic torque T_{e1} is linearly proportional to the q-axis current i_{q1}. When the $d-$axis rotor flux is constant, the maximum electromagnetic torque per ampere can be reached for the field-oriented control at the T_{e1}, proportional to i_{q1}.

2.4. PMSG system

The control block diagram of 2 sets of the same 4-layer recurrent wavelet NN-controlled PMSM direct-driven PMSG system is shown in Figure 3. The wind pattern can be acquired by appropriately programming the PMSM speed. The AC power of the variable frequency and voltage generated by the PMSG system is rectified to DC power by a controllable rectifier. The power converts of the PMSG system direct-driven by a PMSM consist of 2 field-oriented institutions, 2 current control loops, 2 sine pulse-width modulation (PWM) control circuits, 2 interlock and isolated circuits, and 2 insulated-gate bipolar transistor (IGBT) power modules for the rectifier and inverter. The DC bus voltage of the PMSG system direct-driven by a PMSM via a controllable rectifier can be controlled using the first of the recurrent wavelet NN controllers. Next, the inverter, which is controlled using the second of the recurrent wavelet NN controllers, based on field-oriented control, can convert the DC bus voltage into the AC 60-Hz line voltage to provide for the stand-alone load. A 3-phase, 4-pole, 1.5-kW, 220-V, 10-A, 2000-rpm type of PMSG is used for the experimental test in this study. The electric parameters of the PMSG are $R_{s1} = 0.2\Omega$, $L_{d1} = L_{q1} = 6$ mH, and $L_m = 6.2$ mH. A 1-kW, 220-V, 7-A, 2000-rpm type of 3-phase PMSM acts as the prime machine. In practical applications, the pure differentiator may amplify the high-frequency noise, so the stability of the closed-loop PMSG drive system will be greatly affected. Thus, a filter is implemented as an alternative for the pure differentiators shown in Figure 1. It is designed to behave as a pure differentiator for the main low-frequency dynamic signal and become a low-pass filter for the high-frequency signals.
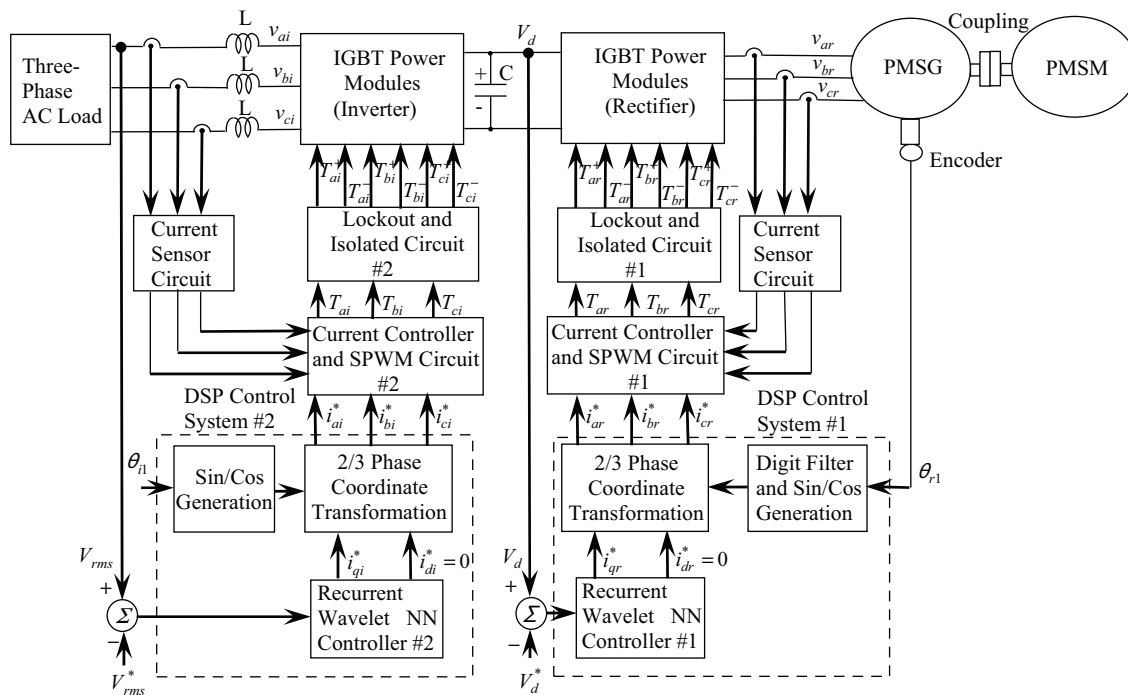

Figure 3. System configuration of the 2 sets of the same recurrent wavelet NN-controlled PMSG system direct-driven by a PMSM with a rectifier and inverter.

The output voltages of the rectifier and inverter controlled by 2 sets of the same recurrent wavelet NN controllers are implemented using 2 independent sets, a TMS320C32 digital signal processor (DSP) control board and an interface card, as seen in Figure 3, where θ_{r1} is the rotor position of the PMSG; i_{dr}^* is the $d-$axis

control current of the rectifier; i_{qr}^* is the $q-$axis control current of the rectifier; i_{ar}^*, i_{br}^*, and i_{cr}^* are the desired phase currents of the PMSG in phases ar, br, and cr, respectively; i_{ar}, i_{br}, and i_{cr} are the actual measured phase currents of the PMSG in phases ar, br, and cr, respectively; T_{ar}, T_{br}, and T_{cr} are the sinusoidal PWM control signals of the rectifier in phases ar, br, and cr, respectively; V_d is the actual measured magnitude of the DC bus voltage in the output end of the rectifier; V_d^* is the desired magnitude of the DC bus voltage in the output end of the rectifier; i_{di}^* is the $d-$axis control current of the inverter; i_{qi}^* is the $q-$axis control current of the inverter; θ_{i1} is the electric angular angle of the inverter, which integrates the command electric angular frequency with respect to t; i_{ai}^*, i_{bi}^*, and i_{ci}^* are the desired phase currents of the inverter in phases ai, bi, and ci, respectively; i_{ai}, i_{bi}, and i_{ci} are the actual measured phase currents of the inverter in phases ai, bi, and ci, respectively; v_{ai}, v_{bi}, and v_{ci} are the actual measured phase voltages of the inverter in phases ai, bi, and ci; respectively; T_{ai}, T_{bi}, and T_{ci} are the sinusoidal PWM control signals of the inverter in phases ai, bi, and ci, respectively; V_{rms} is the actual root-mean-square magnitude of the AC 60-Hz line voltage in the output end of the inverter; and V_{rms}^* is the desired root-mean-square magnitude of the AC 60-Hz line voltage in the output end of the inverter.

3. Recurrent wavelet NN controller

3.1. Description of recurrent wavelet NN

The 2 proposed sets of the same 2-layer recurrent wavelet NNs, with an input layer using feedback signals from the output layer, are taken into account to result in better learning efficiency. The architecture of the 2 sets of the same 4-layer recurrent wavelet NNs, which consists of layer 1, the input layer; layer 2, the mother wavelet layer; layer 3, the wavelet layer; and layer 4, the output layer, is shown in Figure 4. The exciting functions and signal propagations of the nodes in each layer of the recurrent wavelet NN are explained as follows:

Layer 1: **Input layer** i

In layer 1, the input and output signals for each i node in the mth recurrent wavelet NN can be denoted as:

$$nod_{i,m}^1(N) = \prod_o c_{i,m}^1(N) \cdot \mu_{oi,m} \cdot d_{o,m}^4(N-1),$$

$$d_{i,m}^1(N) = g_{i,m}^1(nod_{i,m}^1(N)) = nod_{i,m}^1(N), \quad i = 1,\ 2\ \ and\ \ m = 1,\ 2, \tag{8}$$

where $c_{i,m}^1$ is the input of the ith node in the mth recurrent wavelet NN and $d_{i,m}^1$ is the output of the ith node in the mth recurrent wavelet NN. The different inputs of the 2 sets of recurrent wavelet NNs are $c_{1,1}^1 = e_1 = V_d^* - V_d$, $c_{2,1}^1 = \dot{e}_1$ for the rectifier end of the PMSG system in the first recurrent wavelet NN, and $c_{1,2}^1 = e_2 = V_{rms}^* - V_{rms}$, $c_{2,2}^1 = \dot{e}_2$ for the inverter end of the PMSG system in the second recurrent wavelet NN, respectively. N indicates the number of iterations. The connecting weight $\mu_{oi,m}$ is the recurrent weight between the output layer and the input layer in the mth recurrent wavelet NN. $d_{o,m}^4$ is the output value of the output layer in the mth recurrent wavelet NN.

Layer 2: **Mother wavelet layer** j

In layer 2, each node implements a wavelet $\phi(x)$ that is derived from its mother wavelet. In this paper, the first derivative of the Gaussian wavelet function $net_j^2 = -\frac{(x_i^2 - m_{ij})^2}{(\sigma_{ij})^2}$, $y_j^2 = f_j^2(net_j^2) = \exp(net_j^2)$ is adopted as a mother wavelet. A family of wavelets is constructed by translations and dilations implemented on the

mother wavelet. The input and output for each jth node of this layer in the mth recurrent wavelet NN can be indicated as:
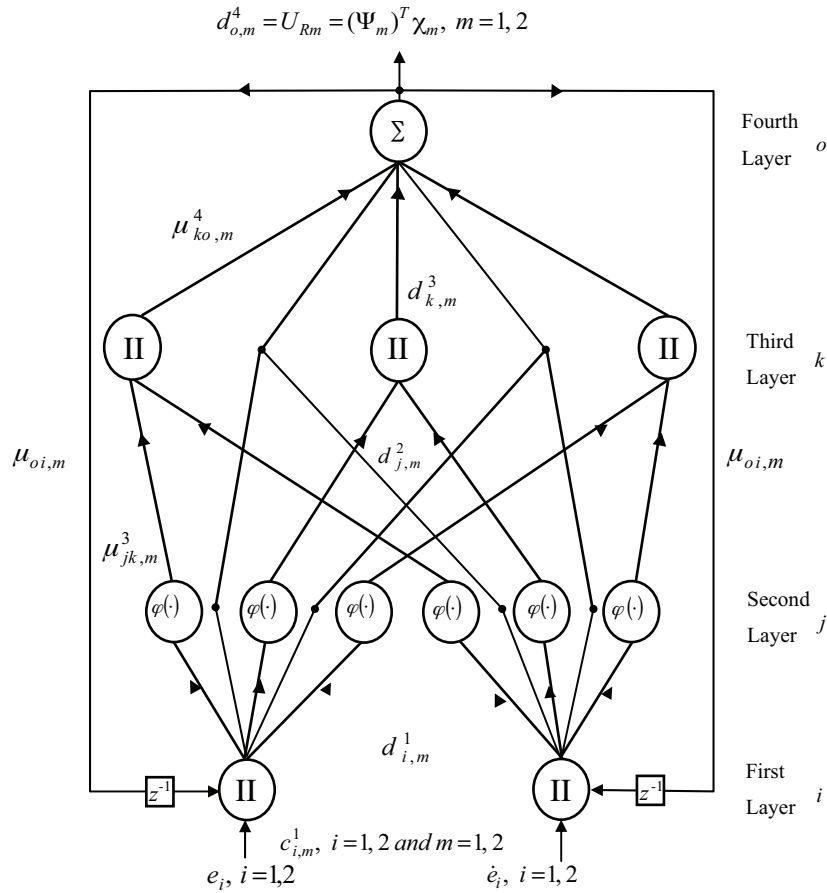
$$d_{o,m}^4 = U_{Rm} = (\Psi_m)^T \chi_m, \ m = 1, 2$$

Figure 4. Structure of the 2 sets of the same 4-layer recurrent wavelet NNs.

$$net_j^2 = -\frac{\left(x_i^2 - m_{ij}\right)^2}{\left(\sigma_{ij}\right)^2}, \ y_j^2 = f_j^2 \left(net_j^2\right) = \exp\left(net_j^2\right) \ net_j^2 = -\frac{\left(x_i^2 - m_{ij}\right)^2}{\left(\sigma_{ij}\right)^2}, \ y_j^2 = f_j^2 \left(net_j^2\right) = \exp\left(net_j^2\right), \quad (9)$$

where $a_{ij,m}$ and $b_{ij,m}$ are the translations and dilations in the jth term of the ith input $c_{i,m}^2$ to the node of the mother wavelet layer in the mth recurrent wavelet NN, and n is the total number of mother wavelets corresponding to the input nodes.

Layer 3: **Wavelet layer** k

In layer 3, the input and output signals for each kth node in the mth recurrent wavelet NN are represented as:

$$nod_{k,m}^3(N) = \prod_j \mu_{jk,m}^3 \cdot c_{j,m}^3(N), \quad d_{k,m}^3(N) = g_{k,m}^3(nod_{k,m}^3(N)) = nod_{k,m}^3(N), \quad k = 1, 2, \cdots, l_1 \ and \ m = 1, 2,$$

$$(10)$$

where $c_{j,m}^3$ represents the jth input to the node of layer 3 in the mth recurrent wavelet NN and $\mu_{jk,m}^3$ is the weight between the mother wavelet layer and the wavelet layer in the mth recurrent wavelet NN. They are supposed to be unity; l_1 is the total number of wavelets if each input node has the same mother wavelet nodes.

***Layer 4:* Output layer o**

In layer 4, the input and output signals for the oth node in the mth recurrent wavelet NN are expressed as:

$$nod_{o,m}^4(N) = \sum_k \mu_{ko,m}^4 \cdot c_{k,m}^4(N), \quad d_{o,m}^4(N) = g_{o,m}^4(nod_{o,m}^4(N)) = nod_{o,m}^4(N), \quad o = 1 \ and \ m = 1,\ 2. \quad (11)$$

The connecting weights $\mu_{ko,m}^4$ are the output action intensity of the oth output associated with the kth node in the mth recurrent wavelet NN; $c_{k,m}^4$ represents the kth input to the node in layer 4 in the mth recurrent wavelet NN. The single oth node in this layer is represented as ?. The outputs in the mth recurrent wavelet NN can be represented as $d_{o,m}^4$.

$$d_{o,m}^4 = (\psi_m)^T \chi_m, \quad m = 1,\ 2 \quad (12)$$

The output values of the 2 sets of the same 4-layer recurrent wavelet NNs can be rewritten as $U_{R\,1} = (\psi_1)^T \chi_1 = i_{qr}^*$ for the rectifier end and $U_{R\,2} = (\psi_2)^T \chi_2 = i_{qi}^*$ for the inverter end. Two vectors, $\psi_1 = \left[\mu_{11,1}^4 \ \mu_{21,1}^4 \ \cdots \ \mu_{l1,1}^4\right]^T$ and $\psi_2 = \left[\mu_{11,2}^4 \ \mu_{21,2}^4 \ \cdots \ \mu_{l1,2}^4\right]^T$, are to be the adjusted parameters between the mother layer and the output layer of the 2 sets of the same 4-layer recurrent wavelet NNs. $\chi_m = \left[c_{1,m}^4 \ c_{2,m}^4 \ \cdots \ c_{l,m}^4\right]^T$, $m = 1,\ 2$ are the inputs vectors in the output layer of the 2 sets of the same 4-layer recurrent wavelet NNs, in which $c_{k,m}^4$ are determined by the selected mother wavelet function and $0 \le c_{k,m}^4 \le 1$. To explain the online learning algorithm of the recurrent wavelet NN using the supervised gradient decent method, first, the energy function $V_{c,m}$ is defined as:

$$V_{c,m} = \frac{1}{2}\,e_m^2, \quad m = 1,\ 2, \quad (13)$$

where e_1 is equal to $V_d^* - V_d$ in the rectifier end of the PMSG system and e_2 is equal to $V_{rms}^* - V_{rms}$ in the inverter end of the PMSG system. Next, the learning algorithm is described as follows:

Layer 4: The propagated error term in the mth recurrent wavelet NN is:

$$v_m^4 = -\frac{\partial V_{c,m}}{\partial nod_{o,m}^4}, \quad m = 1,\ 2\,. \quad (14)$$

Next, the variation $\Delta\mu_{ko,m}^4$ of the connective weights in the mth recurrent wavelet NN can be calculated as:

$$\Delta\mu_{ko,m}^4 = -\gamma_m \frac{\partial V_{c,m}}{\partial d_{o,m}^4} \frac{\partial d_{o,m}^4}{\partial nod_{o,m}^4} \frac{\partial nod_{o,m}^4}{\partial \mu_{ko,m}^4} = -\gamma_m \cdot v_m^4 \cdot c_{k,m}^4, \quad m = 1,\ 2, \quad (15)$$

where γ_m is the learning rate in the mth recurrent wavelet NN. The connective weights $\mu_{ko,m}^4$ in the mth recurrent wavelet NN can be renewed according to the following equation:

$$\mu_{ko,m}^4(N+1) = \mu_{ko,m}^4(N) + \Delta\mu_{ko,m}^4, \quad m = 1,\ 2. \quad (16)$$

Layer 3: To reduce the loading of the computation, all of the connective weights are set as 1 in this layer. The error term in the mth recurrent wavelet NN can be calculated as:

$$v^3_{k,m} \triangleq -\frac{\partial V_{c,m}}{\partial d^4_{o,m}} \frac{\partial d^4_{o,m}}{\partial nod^4_{o,m}} \frac{\partial nod^4_{o,m}}{\partial d^3_{k,m}} \frac{\partial d^3_{k,m}}{\partial nod^3_{k,m}} = v^4_m \cdot \mu^4_{ko,m}(N), \quad m = 1, \ 2. \tag{17}$$

Layer 2: The propagated error term in the mth recurrent wavelet NN is:

$$v^2_{j,m} \triangleq -\frac{\partial V_{c,m}}{\partial d^4_{o,m}} \frac{\partial d^4_{o,m}}{\partial nod^4_{o,m}} \frac{\partial nod^4_{o,m}}{\partial d^3_{k,m}} \frac{\partial d^3_{k,m}}{\partial nod^3_{k,m}} \frac{\partial nod^3_{k,m}}{\partial d^2_{j,m}} \frac{\partial d^2_{j,m}}{\partial nod^2_{j,m}} = \sum_k v^3_{k,m} \cdot d^3_{k,m}(N), \ m = 1, 2. \tag{18}$$

The variation $\Delta a_{ij,m}$ of the translations and the variation $\Delta b_{ij,m}$ of the dilations in the Gaussian wavelet function in the mth recurrent wavelet NN using the chain rule can be calculated as:

$$\begin{aligned} \Rightarrow \Delta m_{ij} &= \left(-\frac{\partial E}{\partial m_{ij}}\right) = \left[-\frac{\partial E}{\partial f^4_o(net^4_o)} \cdot \frac{\partial f^4_o(net^4_o)}{\partial net^4_o} \cdot \frac{\partial net^4_o}{\partial f^3_k(net^3_k)} \cdot \frac{\partial f^3_k(net^3_k)}{\partial net^3_k}\right] \\ &\quad \cdot \left[\frac{\partial net^3_k}{\partial f^2_j(net^2_j)} \cdot \frac{\partial f^2_j(net^2_j)}{\partial net^2_j} \cdot \frac{\partial net^2_j}{\partial m_{ij}}\right] \\ &= \delta^2_j \cdot \frac{2 \cdot (x^2_i - m_{ij})}{(\sigma_{ij})^2} \end{aligned} \tag{19}$$

$$\begin{aligned} \Rightarrow \Delta m_{ij} &= \left(-\frac{\partial E}{\partial m_{ij}}\right) \left[-\frac{\partial E}{\partial f^4_o(net^4_o)} \cdot \frac{\partial f^4_o(net^4_o)}{\partial net^4_o} \cdot \frac{\partial net^4_o}{\partial f^3_k(net^3_k)} \cdot \frac{\partial f^3_k(net^3_k)}{\partial net^3_k}\right] \\ &\quad \cdot \left[\frac{\partial net^3_k}{\partial f^2_j(net^2_j)} \cdot \frac{\partial f^2_j(net^2_j)}{\partial net^2_j} \cdot \frac{\partial net^2_j}{\partial m_{ij}}\right] \\ &= \delta^2_j \cdot \frac{2 \cdot (x^2_i - m_{ij})}{(\sigma_{ij})^2} \end{aligned} \tag{20}$$

The translations $a_{ij,m}$ and dilations b_{ij}, m in the mth recurrent wavelet NN can be renewed according to the following equations:

$$a_{ij,m}(N + 1) = a_{ij,m}(N) + \Delta a_{ij,m}, \ \ m = 1, 2, \tag{21}$$

$$b_{ij,m}(N + 1) = b_{ij,m}(N) + \Delta b_{ij,m}, \ \ m = 1, 2. \tag{22}$$

The variation $\Delta \mu_{oi,m}$ of the recurrent weights in the mth recurrent wavelet NN using the chain rule and the gradient descent method can be renewed as:

$$\Delta \mu_{oi,m} = -\frac{\partial V_{c,m}}{\partial nod^2_{j,m}} \frac{\partial nod^2_{j,m}}{\partial d^1_{i,m}} \frac{\partial d^1_{i,m}}{\partial nod^1_{i,m}} \frac{\partial nod^1_{i,m}}{\partial \mu_{oi,m}}$$

$$= \sum_j \frac{v^2_{j,m}[(c^2_{i,m}(N) \cdot a_{ij,m}) \cdot c^1_{i,m}(N) \cdot {}_i d^4_{o,m}(N-1)]}{b_{ij,m}}, \ \ m = 1, 2. \tag{23}$$

The recurrent weights $\mu_{oi,m}$ in the mth recurrent wavelet NN can be renewed according to the following equation:

$$\mu_{oi,m}(N + 1) = \mu_{oi,m}(N) + \Delta \mu_{oi,m}, \ \ m = 1, 2. \tag{24}$$

Due to the uncertainty effect of the system dynamics, the accurate computation of the Jacobian $\frac{\partial V_{c,m}}{\partial d^4_{o,m}}$, $m = 1, 2$ in the PMSG system cannot be determined. To dispel the difficulty and handle the above matter, use of

the delta adaptation law [44] can raise the online learning capacity of the connective weights. Therefore, the delta adaptation law can be calculated as:

$$v_m^4 = e_m + \dot{e}_m, \quad m = 1,\, 2. \tag{25}$$

3.2. Convergence analyses

The selection of the values for the learning-rate parameters has a significant effect on the network performance. In order to train the recurrent wavelet NN effectively, the varied learning rate, which guarantees the convergence of the output error based on the analyses of a discrete-type Lyapunov function, is derived in this section. The convergence analysis in this study is to derive a specific learning-rate parameter for specific types of network parameters to assure the convergence of the output error [35].

Theorem 1 Let γ_m be the learning-rate parameter of the mth recurrent wavelet NN and let $P_{w\,max,m}$ be defined as $P_{w\,max,m} \equiv max_N \|P_{w,m}(N)\|$, where $P_{w,m}(N) = \partial d_{o,m}^4 / \partial \mu_{ko,m}^4$ in the mth recurrent wavelet NN and $\|\cdot\|$ is the Euclidean norm in $\Re^n$. The convergence is guaranteed if γ_m is chosen as $\gamma_m = \lambda_m / (P_{w\,max,m}^2) = \lambda_m / R_{u,m}$, in which λ_m is a positive constant gain and $R_{u,m}$ is the number of nodes in wavelet layer of the mth recurrent wavelet NN.

Proof. Since

$$P_{w,m}(N) = \frac{\partial d_{o,m}^4}{\partial \mu_{ko,m}^4} = c_{k,m}^4, \tag{26}$$

thus

$$\|P_{w,m}(N)\| < \sqrt{R_{u,m}}. \tag{27}$$

Next, a discrete-type Lyapunov function is selected as:

$$V_m(N) = \frac{1}{2} e_m^2(N). \tag{28}$$

The change in the Lyapunov function is obtained by:

$$\Delta V_m(N) = V_m(N+1) - V_m(N) = \frac{1}{2}\left[e_m^2(N+1) - e_m^2(N)\right]. \tag{29}$$

The error difference can be represented by [35]:

$$e_m(N+1) = e_m(N) + \Delta e_m(N) = e_m(N) + \left[\frac{\partial e_m(N)}{\partial \mu_{ko,m}^4}\right]^T \Delta \mu_{ko,m}^4, \tag{30}$$

where $\Delta \mu_{ko,m}^4$ represents a weight change in the output layer. Using Eqs. (14), (15), and (30), then:

$$\frac{\partial e_m(N)}{\partial \mu_{ko,m}^4} = \frac{\partial e_m(N)}{\partial d_{o,m}^4} \frac{\partial d_{o,m}^4}{\partial \mu_{ko,m}^4} = -\frac{v_{o,m}^4}{e_m(N)} P_{w,m}(N), \tag{31}$$

$$e_m(N+1) = e_m(N) - \left[\frac{\mu_{o,m}^4}{e_m(N)} P_{w,m}(N)\right]^T \gamma_m \mu_{o,m}^4 P_{w,m}(N). \tag{32}$$

Then:

$$
\begin{aligned}
\|e_m\,(N+1)\| &= \left\| e_m\,(N) \left[1 - \gamma_m \left(\mu_{o,m}^4 \big/ e_m\,(N) \right)^2 P_{w,m}^T\,(N)\,P_{w,m}\,(N) \right] \right\| \\
&\leq \|e\,(N)\| \left\| 1 - \gamma_m \left(\mu_{o,m}^4 \big/ e_m\,(N) \right)^2 P_{w,m}^T\,(N)\,P_{w,m}\,(N) \right\|
\end{aligned}
. \tag{33}
$$

If η_w is chosen as $\lambda_m = \lambda_m \big/ (P_{w\,max,m}^2) = \lambda_m / R_{u,m}$, the term $\left\| 1 - \gamma_m \left(\mu_{o,k}^4 \big/ e_m\,(N) \right)^2 P_{w,m}^T\,(N)\,P_{w,m}\,(N) \right\|$
in Eq. (33) is less than 1. Therefore, the Lyapunov stability of $V_m > 0$ and $\Delta V_m < 0$ is guaranteed. The output error between the reference model and the actual system will converge to 0, as $t \to \infty$. This completes the proof of the theorem.

Remark The values of the learning rate parameter γ_m are dependent on the selection of the value λ_m.

4. Experimental results

The 2 sets of the same recurrent wavelet NN-controlled PMSG system are realized in 2 sets of the TMS320C32 DSP control system. A photo of the experimental set up is shown in Figure 5. To implement the current-controlled PWM rectifier and inverter by field-oriented control, 2 sets of BSM 100GB 120DLC IGBT power modules, manufactured by Eupec Co., are adopted in this study. The switching frequency of both IGBT power modules is 15 kHz. The 2 programs of the 2 sets of the TMS320C32 DSP control system used for executing the 2 sets of the same recurrent wavelet NNs and online training of the 2 sets of the same recurrent wavelet
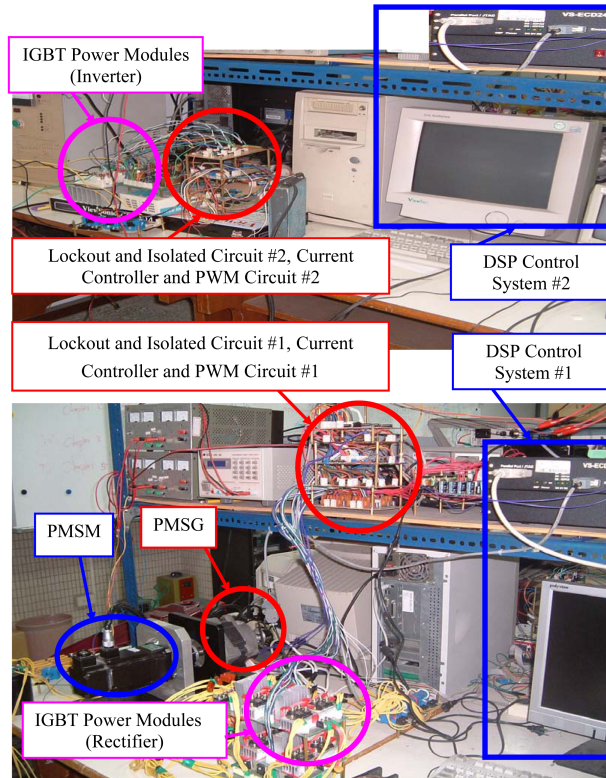

Figure 5. Photo of the experimental set up.

NNs need 2-ms sampling intervals. Furthermore, to show the effectiveness of the control system and training performance, the 2 kinds of recurrent wavelet NNs with 2 different nodes are provided in the experimentation. The first kind of recurrent wavelet NN has 2, 10, 5, and 1 nodes in layers 1, 2, 3, and 4, respectively. The second kind of recurrent wavelet NN has 2, 14, 7, and 1 nodes in layers 1, 2, 3, and 4, respectively. To initialize the
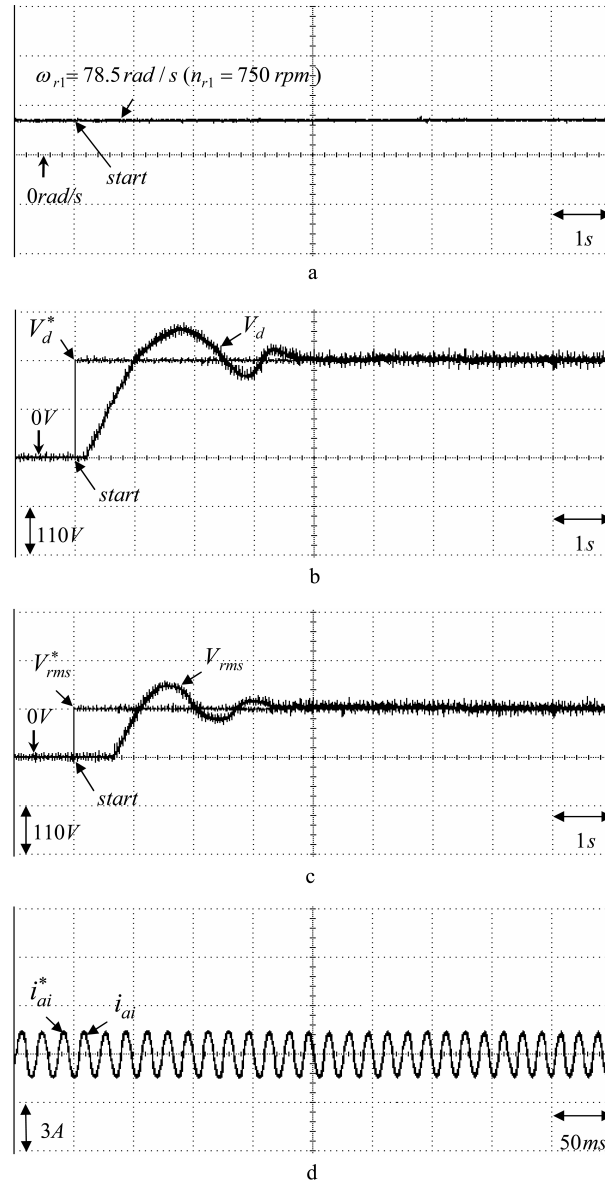

Figure 6. Experimental results of the PMSM direct-drive PMSG system using the PI controller for the Δ connection 3-phase loads of 100 Ω, with ω_{r1} = 78.5 rad/s (n_{r1} = 750 rpm) in case 1: a) rotor speed $\omega_{r1}(n_{r1})$; b) adjusting responses of the step desired magnitude V_d^* of the DC bus voltage and actual measured magnitude V_d of the DC bus voltage in the output end of the rectifier; c) adjusting responses of the step desired root-mean-square magnitude V_{rms}^* of the AC 60-Hz line voltage and actual measured root-mean-square magnitude V_{rms} of the AC 60-Hz line voltage in the output end of the inverter V_{rms}; and d) tracking responses of the desired phase current i_{ai}^* and actual measured phase current i_{ai} in phase ai of the inverter.

parameters of the wavelets, the initialization of the recurrent wavelet NN parameters is adopted reference [45]. The effect due to the inaccurate selection of the initialized parameters can be retrieved by the online parameter training methodology. The parameter adjustment process remains continually active for the duration of the experimentation. To verify the control performance of the proposed 2 sets of the same recurrent wavelet NN-controlled PMSG system direct-driven by a PMSM based on a wind turbine emulator, 2 cases with field-oriented control currents of $i_{di}^* = 0A$ and $i_{dr}^* = 0A$ are tested. To show the adjusting and tracking responses for the stand-alone power application, 3 cases are selected. Case 1 is the Δ connection 3-phase load 100 Ω and the rotor speed ω_{r1} (n_{r1}), step desired magnitude V_d^* of the DC bus voltage, and step desired root-mean-square magnitude V_{rms}^* of the AC 60-Hz line voltage are set as 78.5 rad/s (750 rpm), 220 V, and 110 V, respectively. Case 2 is the Δ connection 3-phase load 50 Ω and the rotor speed ω_{r1}, desired magnitude V_d^* of the DC bus voltage, and desired root-mean-square magnitude V_{rms}^* of the AC 60-Hz line voltage are set as 157 rad/s (n_{r1} = 1500 rpm), 220 V, and 110 V, respectively. Case 3 is the Δ connection 3-phase load 18 Ω and the rotor speed ω_{r1}, desired magnitude V_d^* of the DC bus voltage, and desired root-mean-square magnitude V_{rms}^* of the AC 60-Hz line voltage are set as 209.3 rad/s (2000 rpm), 220 V, and 110 V, respectively. The Δ connection 3-phase loads of the 100 Ω, 50 Ω, and 18 Ω dispatched powers are 121 W, 242 W, and 672 W, respectively. Some experimental results of the PI-controlled PMSM direct-drive PMSG system are demonstrated for the comparison of the control performance. Since the PMSG system is a nonlinear time-varying system, the gains of the PI controllers for both the DC bus voltage adjustment and AC 60-Hz line voltage adjustment are obtained by trial and error to achieve steady-state control performance. The control gains are $K_p = 5.2$, $K_i = 10.2$ for the DC bus voltage adjustment and $K_p = 4.8$, $K_i = 10.8$ for the AC 60-Hz line voltage adjustment in the 2 sets of PI controllers. The experimental results of the PI-controlled PMSM direct-driven PMSG system for the Δ connection 3-phase loads of 100 Ω with ω_{r1} = 78.5 rad/s (n_{r1} = 750 rpm) in case 1 are shown in Figure 6, where the rotor speed ω_{r1} (n_{r1}) is shown in Figure 6a; the adjusting responses of the step desired magnitude V_d^* of the DC bus voltage and actual measured magnitude V_d of the DC bus voltage in the output end of the rectifier are shown in Figure 6b; the adjusting responses of the step desired root-mean-square magnitude V_{rms}^* of the AC 60-Hz line voltage and actual measured root-mean-square magnitude V_{rms} of the AC 60-Hz line voltage in the output end of the inverter are shown in Figure 6c; and the tracking responses of the desired phase current i_{ai}^* and actual measured phase current i_{ai} in phase ai of the inverter are shown in Figure 6d. The experimental results of the PI-controlled PMSM direct-driven PMSG system for the Δ connection 3-phase loads of 50 Ω with ω_{r1} = 150 rad/s (n_{r1} = 1500 rpm) in case 2 are shown in Figure 7, where the rotor speed $\omega_{r1}(n_{r1})$ is shown in Figure 7a; the adjusting responses of the step desired magnitude V_d^* of the DC bus voltage and actual measured magnitude V_d of the DC bus voltage in the output end of the rectifier are shown in Figure 7b; the adjusting responses of the step desired root-mean-square magnitude V_{rms}^* of the AC 60-Hz line voltage and actual measured root-mean-square magnitude V_{rms} of the AC 60-Hz line voltage in the output end of the inverter are shown in Figure 7c; and the tracking responses of the desired phase current i_{ai}^* and actual measured phase current i_{ai} in phase ai of the inverter are shown in Figure 7d. The experimental results of the PI-controlled PMSM direct-drive PMSG system for the Δ connection 3-phase loads of 18 Ω with ω_{r1} = 209.3 rad/s (n_{r1} = 2000 rpm) in case 3 are shown in Figure 8, where the rotor speed $\omega_{r1}(n_{r1})$ is shown in Figure 8a; the adjusting responses of the step desired magnitude V_d^* of the DC bus voltage and actual measured magnitude V_d of the DC bus voltage in the output end of the rectifier are shown in Figure 8b; the adjusting responses of the step desired root-mean-square magnitude V_{rms}^* of the AC 60-Hz line voltage and actual measured root-mean-square magnitude V_{rms} of the AC 60-Hz line voltage in the output end of the inverter are shown in Figure 8c;

and the tracking responses of the desired phase current i_{ai}^* and actual measured phase current i_{ai} in phase ai of the inverter are shown in Figure 8d. From the experimental results, sluggish DC bus voltage and AC 60-Hz line voltage adjusting responses are obtained for the PI-controlled PMSM direct-drive PMSG system because of the weak robustness of the linear controller.
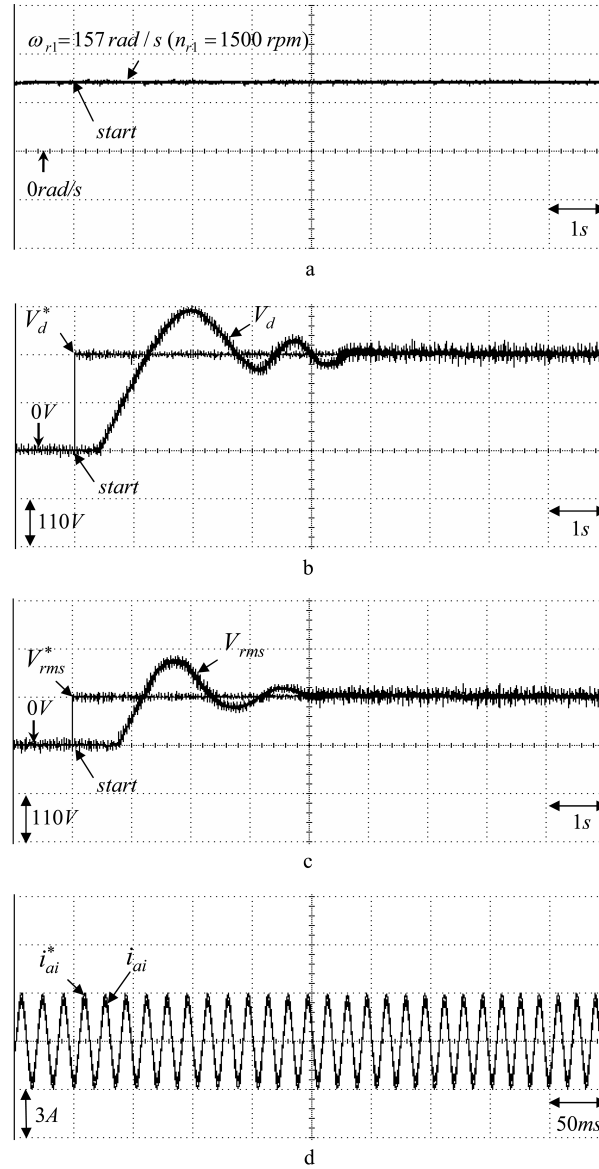

Figure 7. Experimental results of the PMSM direct-drive PMSG system using the PI controller for the Δ connection 3-phase loads of 50 Ω with ω_{r1} =157 rad/s (n_{r1} = 1500 rpm) in case 2: a) rotor speed $\omega_{r1}(n_{r1})$; b) adjusting responses of the step desired magnitude V_d^* of the DC bus voltage and actual measured magnitude V_d of the DC bus voltage in the output end of the rectifier; c) adjusting responses of the step desired root-mean-square magnitude V_{rms}^* of the AC 60-Hz line voltage and actual measured root-mean-square magnitude V_{rms} of the AC 60-Hz line voltage in the output end of the inverter V_{rms}; and d) tracking responses of the desired phase current i_{ai}^* and actual measured phase current i_{ai} in phase ai of the inverter.
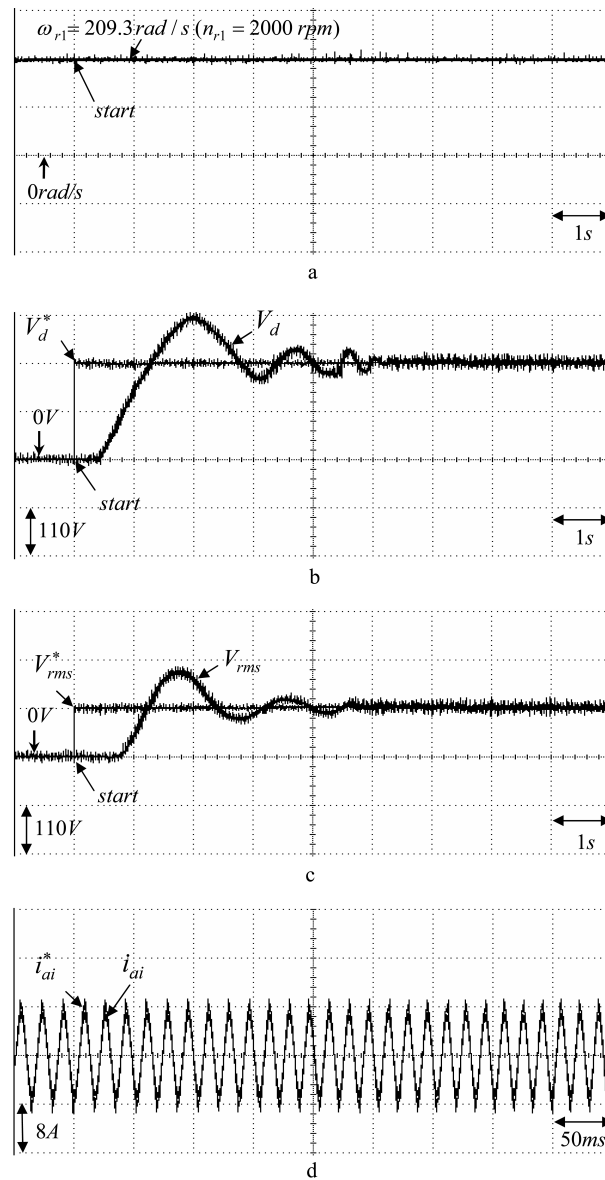
Figure 8. Experimental results of the PMSM direct-drive PMSG system using the PI controller for the Δ connection 3-phase loads of 18 Ω with ω_{r1} = 209.3 rad/s (n_{r1} =2000 rpm) in case 3: a) rotor speed $\omega_{r1}(n_{r1})$; b) adjusting responses of the step desired magnitude V_d^* of the DC bus voltage and actual measured magnitude V_d of the DC bus voltage in the output end of the rectifier; c) adjusting responses of the step desired root-mean-square magnitude V_{rms}^* of the AC 60-Hz line voltage and actual measured root-mean-square magnitude V_{rms} of the AC 60-Hz line voltage in the output end of the inverter V_{rms}; and d) tracking responses of the desired phase current i_{ai}^* and actual measured phase current i_{ai} in phase ai of the inverter.

Some experimental results of the PMSM direct-drive PMSG system using the conventional NN controller with 2, 5, and 1 neurons in the input layer, the hidden layer with a sigmoid function, and the output layer for the Δ connection 3-phase loads of 100 Ω with ω_{r1} = 78.5 rad/s (n_{r1} = 750 rpm) in case 1 are shown in Figure 9, where the rotor speed ω_{r1} (n_{r1}) is shown in Figure 9a; the adjusting responses of the step desired magnitude V_d^* of the DC bus voltage and actual measured magnitude V_d of the DC bus voltage in the output end of

the rectifier are shown in Figure 9b; the adjusting responses of the step desired root-mean-square magnitude V_{rms}^* of the AC 60-Hz line voltage and actual measured root-mean-square magnitude V_{rms} of the AC 60-Hz line voltage in the output end of the inverter are shown in Figure 9c; and the tracking responses of the desired phase current i_{ai}^* and actual measured phase current i_{ai} in phase ai of the inverter are shown in Figure 9d.
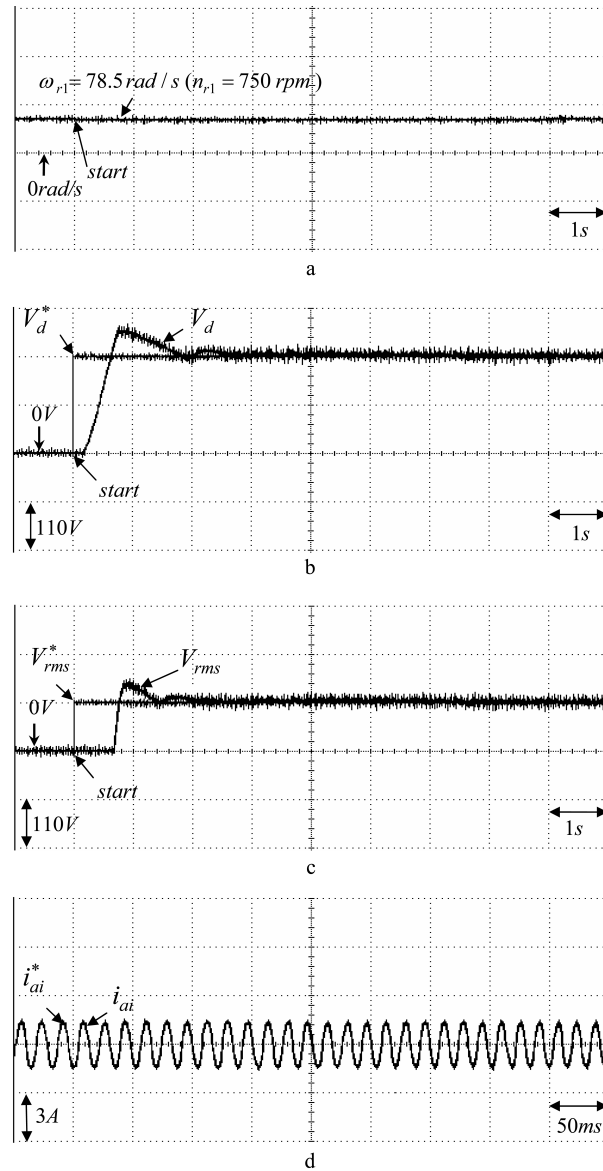

Figure 9. Experimental results of the PMSM direct-drive PMSG system using the conventional NN controller for the Δ connection 3-phase loads of 100 Ω with ω_{r1} = 78.5 rad/s (n_{r1} = 750 rpm) in case 1: a) rotor speed $\omega_{r1}(n_{r1})$; b) adjusting responses of the step desired magnitude V_d^* of the DC bus voltage and actual measured magnitude V_d of the DC bus voltage in the output end of the rectifier; c) adjusting responses of the step desired root-mean-square magnitude V_{rms}^* of the AC 60-Hz line voltage and actual measured root-mean-square magnitude V_{rms} of the AC 60-Hz line voltage in the output end of the inverter V_{rms}; and d) tracking responses of the desired phase current i_{ai}^* and actual measured phase current i_{ai} in phase ai of the inverter.

The experimental results of the PMSM direct-drive PMSG system using the conventional NN controller for the Δ connection 3-phase loads of 50 Ω with ω_{r1} = 150 rad/s (n_{r1} = 1500 rpm) in case 2 are shown in Figure 10, where the rotor speed $\omega_{r1}(n_{r1})$ is shown in Figure 10a; the adjusting responses of the step desired magnitude V_d^* of the DC bus voltage and actual measured magnitude V_d of the DC bus voltage in the output end of the

Figure 10. Experimental results of the PMSM direct-drive PMSG system using the conventional NN controller for the Δ connection 3-phase loads of 50 Ω with ω_{r1} = 157 rad/s (n_{r1} = 1500 rpm) in case 2: a) rotor speed $\omega_{r1}(n_{r1})$; b) adjusting responses of the step desired magnitude V_d^* of the DC bus voltage and actual measured magnitude V_d of the DC bus voltage in the output end of the rectifier; c) adjusting responses of the step desired root-mean-square magnitude V_{rms}^* of the AC 60-Hz line voltage and actual measured root-mean-square magnitude V_{rms} of the AC 60-Hz line voltage in the output end of the inverter V_{rms}; and d) tracking responses of the desired phase current i_{ai}^* and actual measured phase current i_{ai} in phase ai of the inverter.
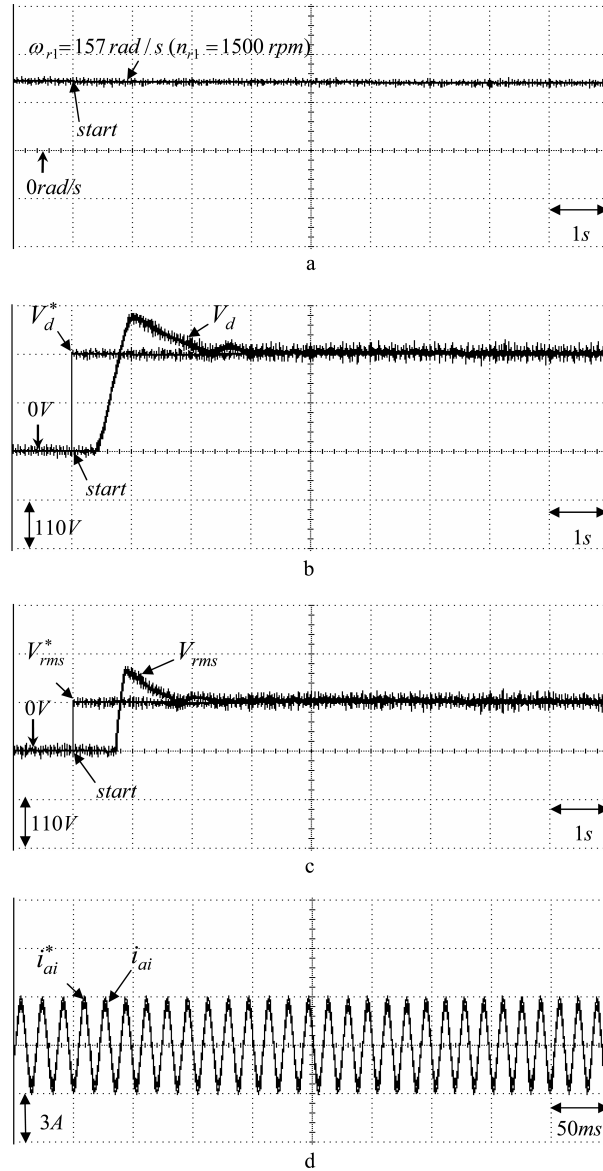
rectifier are shown in Figure 10b; the adjusting responses of step desired root-mean-square magnitude V_{rms}^* of the AC 60-Hz line voltage and actual measured root-mean-square magnitude V_{rms} of the AC 60-Hz line voltage in the output end of the inverter are shown in Figure 10c; and the tracking responses of the desired phase current i_{ai}^* and actual measured phase current i_{ai} in phase ai of the inverter are shown in Figure 10d. The
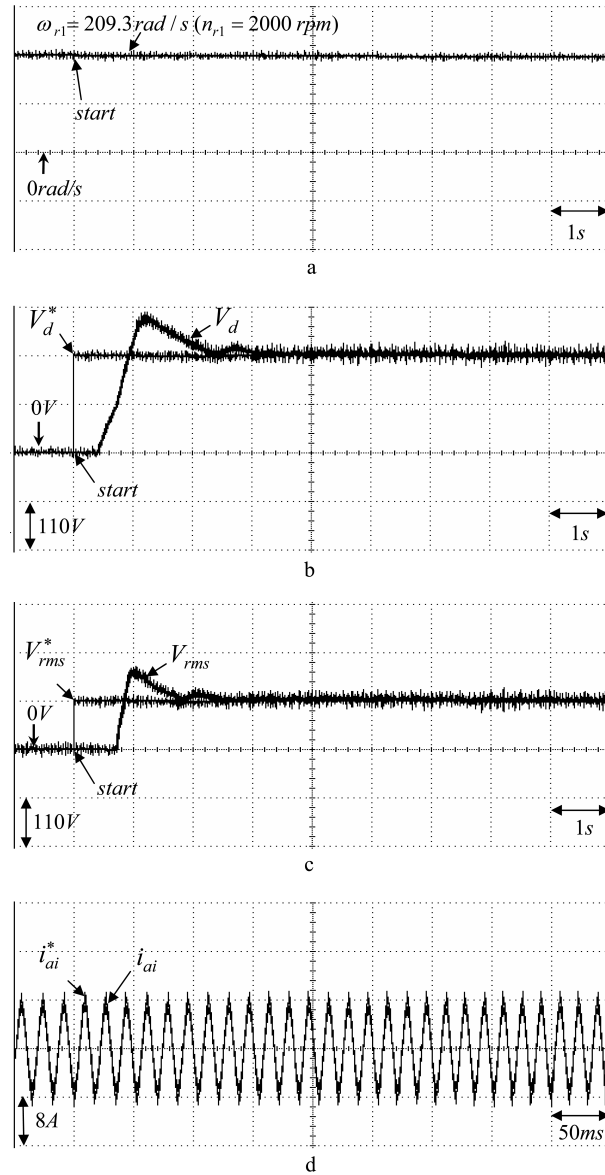

Figure 11. Experimental results of the PMSM direct-drive PMSG system using the conventional NN controller for the Δ connection 3-phase loads of 18 Ω with ω_{r1} =209.3 rad/s (n_{r1} = 2000 rpm) in case 3: a) rotor speed $\omega_{r1}(n_{r1})$; b) adjusting responses of the step desired magnitude V_d^* of the DC bus voltage and actual measured magnitude V_d of the DC bus voltage in the output end of the rectifier; c) adjusting responses of the step desired root-mean-square magnitude V_{rms}^* of the AC 60-Hz line voltage and actual measured root-mean-square magnitude V_{rms} of the AC 60-Hz line voltage in the output end of the inverter V_{rms}; and d) tracking responses of the desired phase current i_{ai}^* and actual measured phase current i_{ai} in phase ai of the inverter.

experimental results of the PMSM direct-drive PMSG system using the conventional NN controller for the Δ connection 3-phase loads of 18 Ω with ω_{r1} = 209.3 rad/s (n_{r1} = 2000 rpm) in case 3 are shown in Figure 11, where the rotor speed $\omega_{r1}(n_{r1})$ is shown in Figure 11a; the adjusting responses of the step desired magnitude V_d^* of the DC bus voltage and actual measured magnitude V_d of the DC bus voltage in the output end of the rectifier are shown in Figure 11b; the adjusting responses of the step desired root-mean-square magnitude V_{rms}^* of the AC 60-Hz line voltage and actual measured root-mean-square magnitude V_{rms} of the AC 60-Hz line voltage in the output end of the inverter are shown in Figure 11c; and the tracking responses of the desired phase current i_{ai}^* and actual measured phase current i_{ai} in phase ai of the inverter are shown in Figure 11d. From the experimental results, a few sluggish DC bus voltage and AC 60-Hz line voltage adjusting responses are obtained for the PI-controlled PMSM direct-drive PMSG system because of the weak robustness of the linear controller.

Some experimental results of the proposed recurrent wavelet NN-controlled PMSM direct-drive PMSG system are discussed. The experimental results of the PMSM direct-drive PMSG system using the first kind of recurrent wavelet NN controller for the Δ connection 3-phase loads of 100 Ω with ω_{r1} = 78.5 rad/s (n_{r1} = 750 rpm) in case 1 are shown in Figure 12, where the rotor speed $\omega_{r1}(n_{r1})$ is shown in Figure 12a; the adjusting responses of the step desired magnitude V_d^* of the DC bus voltage and actual measured magnitude V_d of the DC bus voltage in the output end of the rectifier are shown in Figure 12b; the adjusting responses of the step desired root-mean-square magnitude V_{rms}^* of the AC 60-Hz line voltage and actual measured root-mean-square magnitude V_{rms} of the AC 60-Hz line voltage in the output end of the inverter are shown in Figure 12c; and the tracking responses of the desired phase current i_{ai}^* and actual measured phase current i_{ai} in phase ai of the inverter are shown in Figure 12d. The experimental results of the PMSM direct-drive PMSG system using the first kind of recurrent wavelet NN controller for the Δ connection 3-phase loads of 50 Ω with ω_{r1} = 150 rad/s (n_{r1} = 1500 rpm) in case 2 are shown in Figure 13, where the rotor speed $\omega_{r1}(n_{r1})$ is shown in Figure 13a; the adjusting responses of the step desired magnitude V_d^* of the DC bus voltage and actual measured magnitude V_d of the DC bus voltage in the output end of the rectifier are shown in Figure 13b; the adjusting responses of the step desired root-mean-square magnitude V_{rms}^* of the AC 60-Hz line voltage and actual measured root-mean-square magnitude V_{rms} of the AC 60-Hz line voltage in the output end of the inverter are shown in Figure 13c; and the tracking responses of the desired phase current i_{ai}^* and actual measured phase current i_{ai} in phase ai of the inverter are shown in Figure 13d. The experimental results of the PMSM direct-drive PMSG system using the first kind of recurrent wavelet NN controller for the Δ connection 3-phase loads of 18 Ω with ω_{r1} = 209.3 rad/s (n_{r1} = 2000 rpm) in case 3 are shown in Figure 14, where the rotor speed $\omega_{r1}(n_{r1})$ is shown in Figure 14a; the adjusting responses of the step desired magnitude V_d^* of the DC bus voltage and actual measured magnitude V_d of the DC bus voltage in the output end of the rectifier are shown in Figure 14b; the adjusting responses of the step desired root-mean-square magnitude V_{rms}^* of the AC 60-Hz line voltage and actual measured root-mean-square magnitude V_{rms} of the AC 60-Hz line voltage in the output end of the inverter are shown in Figure 14c; and the tracking responses of the desired phase current i_{ai}^* and actual measured phase current i_{ai} in phase ai of the inverter are shown in Figure 14d. The experimental results of the PMSM direct-drive PMSG system using the second kind of recurrent wavelet NN controller for the Δ connection 3-phase loads of 100 Ω with ω_{r1} = 78.5 rad/s (n_{r1} = 750 rpm) in case 1 are shown in Figure 15, where the rotor speed $\omega_{r1}(n_{r1})$ is shown in Figure 15a; the adjusting responses of the step desired magnitude V_d^* of the DC bus voltage and actual measured magnitude V_d of the DC bus voltage in the output end of the rectifier are shown in Figure 15b; the adjusting responses of the step desired root-mean-square

magnitude V_{rms}^* of the AC 60-Hz line voltage and actual measured root-mean-square magnitude V_{rms} of the AC 60-Hz line voltage in the output end of the inverter are shown in Figure 15c; and the tracking responses of the desired phase current i_{ai}^* and actual measured phase current i_{ai} in phase ai of the inverter are shown in Figure 15d. The experimental results of the PMSM direct-drive PMSG system using the second kind of
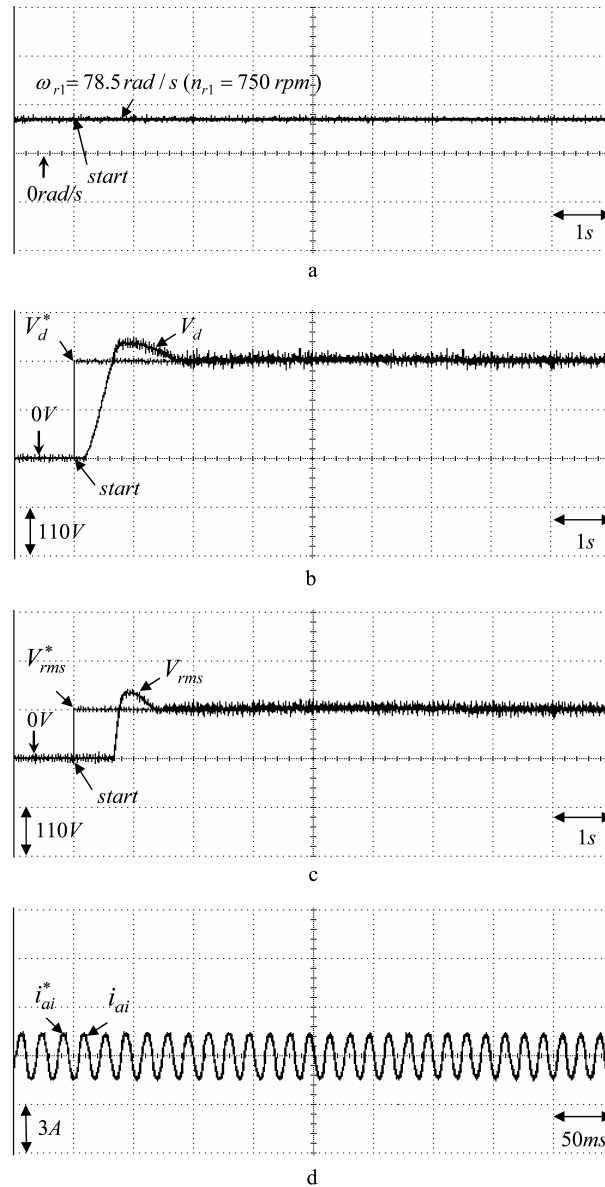

Figure 12. Experimental results of the PMSM direct-drive PMSG system using the first kind of recurrent wavelet NN controller for the Δ connection 3-phase loads of 100 Ω with ω_{r1} = 78.5 rad/s (n_{r1} = 750 rpm) in case 1: a) rotor speed $\omega_{r1}(n_{r1})$; b) adjusting responses of the step desired magnitude V_d^* of the DC bus voltage and actual measured magnitude V_d of the DC bus voltage in the output end of the rectifier; c) adjusting responses of the step desired root-mean-square magnitude V_{rms}^* of the AC 60-Hz line voltage and actual measured root-mean-square magnitude V_{rms} of the AC 60-Hz line voltage in the output end of the inverter V_{rms}; and d) tracking responses of the desired phase current i_{ai}^* and actual measured phase current i_{ai} in phase ai of the inverter.

recurrent wavelet NN controller for the Δ connection 3-phase loads of 50 Ω with ω_{r1} = 150 rad/s (n_{r1} = 1500 rpm) in case 2 are shown in Figure 16, where the rotor speed $\omega_{r1}(n_{r1})$ is shown in Figure 16a; the adjusting responses of the step desired magnitude V_d^* of the DC bus voltage and actual measured magnitude V_d of the DC bus voltage in the output end of the rectifier are shown in Figure 16b; the adjusting responses of step
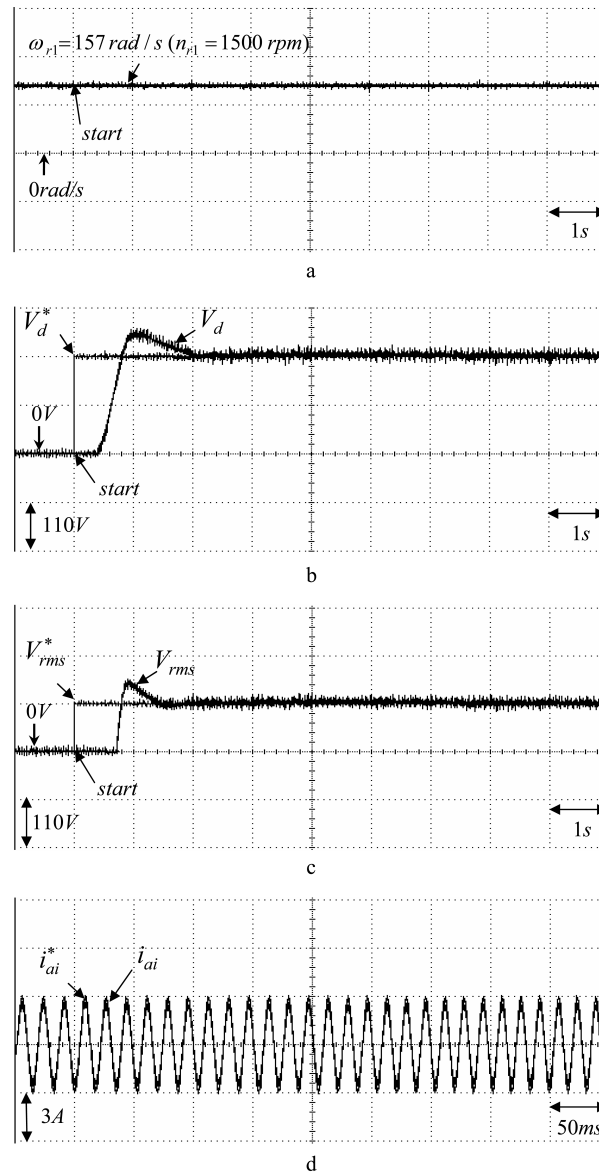

Figure 13. Experimental results of the PMSM direct-drive PMSG system using the first kind of recurrent wavelet NN controller for the Δ connection 3-phase loads of 50 Ω with ω_{r1} = 157 rad/s (n_{r1} = 1500 rpm) in case 2: a) rotor speed $\omega_{r1}(n_{r1})$; b) adjusting responses of the step desired magnitude V_d^* of the DC bus voltage and actual measured magnitude V_d of the DC bus voltage in the output end of the rectifier; c) adjusting responses of the step desired root-mean-square magnitude V_{rms}^* of the AC 60-Hz line voltage and actual measured root-mean-square magnitude V_{rms} of the AC 60-Hz line voltage in the output end of the inverter V_{rms}; and d) tracking responses of the desired phase current i_{ai}^* and actual measured phase current i_{ai} in phase ai of the inverter.

desired root-mean-square magnitude V_{rms}^* of the AC 60-Hz line voltage and actual measured root-mean-square magnitude V_{rms} of the AC 60-Hz line voltage in the output end of the inverter are shown in Figure 16c; and the tracking responses of the desired phase current i_{ai}^* and actual measured phase current i_{ai} in phase ai of the inverter are shown in Figure 16d. The experimental results of the PMSM direct-drive PMSG system using
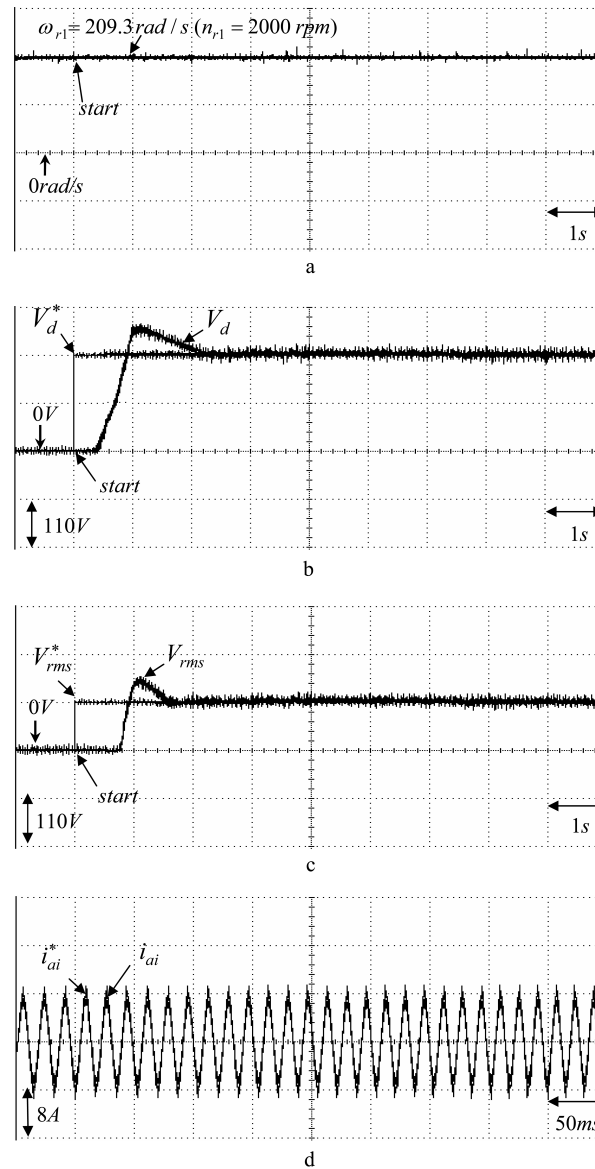

Figure 14. Experimental results of the PMSM direct-drive PMSG system using the first kind of recurrent wavelet NN controller for the Δ connection 3-phase loads of 18 Ω with $\omega_{r1} = 209.3$ rad/s ($n_{r1} = 2000$ rpm) in case 3: a) rotor speed $\omega_{r1}(n_{r1})$; b) adjusting responses of step desired magnitude V_d^* of the DC bus voltage and actual measured magnitude V_d of the DC bus voltage in the output end of the rectifier; c) adjusting responses of the step desired root-mean-square magnitude V_{rms}^* of the AC 60-Hz line voltage and actual measured root-mean-square magnitude V_{rms} of the AC 60-Hz line voltage in the output end of the inverter V_{rms}; and d) tracking responses of the desired phase current i_{ai}^* and actual measured phase current i_{ai} in phase ai of the inverter.

the second kind of recurrent wavelet NN controller for the Δ connection 3-phase loads of 18 Ω with ω_{r1} = 209.3 rad/s (n_{r1} = 2000 rpm) in case 3 are shown in Figure 17, where the rotor speed $\omega_{r1}(n_{r1})$ is shown in Figure 17a; the adjusting responses of step desired magnitude V_d^* of the DC bus voltage and actual measured magnitude V_d of the DC bus voltage in the output end of the rectifier are shown in Figure 17b; the adjusting
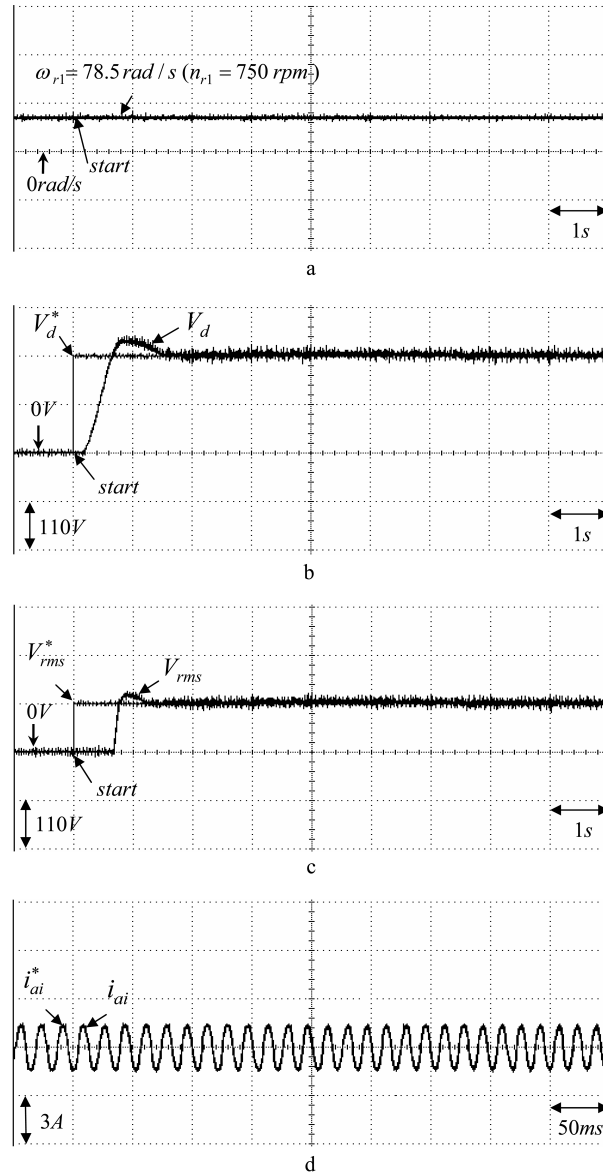

Figure 15. Experimental results of the PMSM direct-drive PMSG system using the second kind of recurrent wavelet NN controller for the Δ connection 3-phase loads of 100 Ω with ω_{r1} = 78.5 rad/s (n_{r1} = 750 rpm) in case 1: a) rotor speed $\omega_{r1}(n_{r1})$; b) adjusting responses of the step desired magnitude V_d^* of the DC bus voltage and actual measured magnitude V_d of the DC bus voltage in the output end of the rectifier; c) adjusting responses of the step desired root-mean-square magnitude V_{rms}^* of the AC 60-Hz line voltage and actual measured root-mean-square magnitude V_{rms} of the AC 60-Hz line voltage in the output end of the inverter V_{rms}; and d) tracking responses of the desired phase current i_{ai}^* and actual measured phase current i_{ai} in phase ai of the inverter.

responses of step desired root-mean-square magnitude V_{rms}^* of the AC 60-Hz line voltage and actual measured root-mean-square magnitude V_{rms} of the AC 60-Hz line voltage in the output end of the inverter are shown in Figure 17c; and the tracking responses of the desired phase current i_{ai}^* and actual measured phase current i_{ai} in phase ai of the inverter are shown in Figure 17d. The overshoot and undershoot in the DC bus voltage and
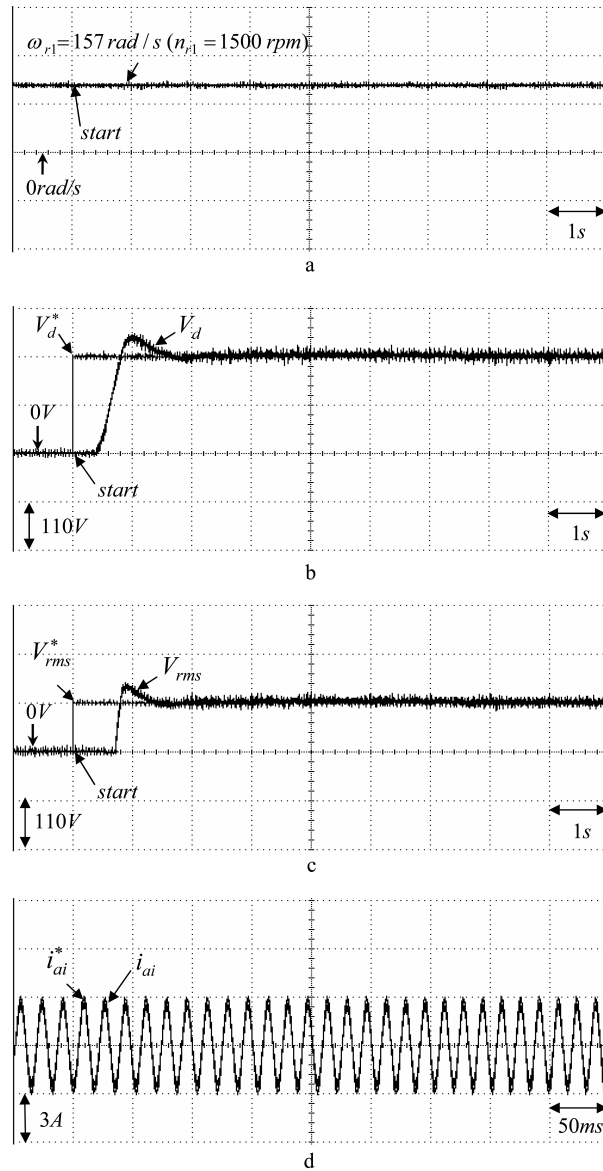

Figure 16. Experimental results of the PMSM direct-drive PMSG system using the second kind of recurrent wavelet NN controller for the Δ connection 3-phase loads of 50 Ω with ω_{r1} = 157 rad/s (n_{r1} = 1500 rpm) in case 2: a) rotor speed $\omega_{r1}(n_{r1})$; b) adjusting responses of the step desired magnitude V_d^* of the DC bus voltage and actual measured magnitude V_d of the DC bus voltage in the output end of the rectifier; c) adjusting responses of the step desired root-mean-square magnitude V_{rms}^* of the AC 60-Hz line voltage and actual measured root-mean-square magnitude V_{rms} of the AC 60-Hz line voltage in the output end of the inverter V_{rms}; and d) tracking responses of the desired phase current i_{ai}^* and actual measured phase current i_{ai} in phase ai of the inverter.

AC 60-Hz line voltage at different rotor speeds using the 2 proposed kinds of recurrent wavelet NN controllers (shown in Figures 12b, 12c, 13b, 13c, 14b, 14c, 15b, 15c, 16b, 16c, 17b, and 17c) are at a lower magnitude and are much more improved than those using the PI controller (shown in Figures 6b, 6c, 7b, 7c, 8b, and 8c) and the conventional NN controller (shown in Figures 9b, 9c, 10b, 10c, 11b, and 11c). Moreover, compared with
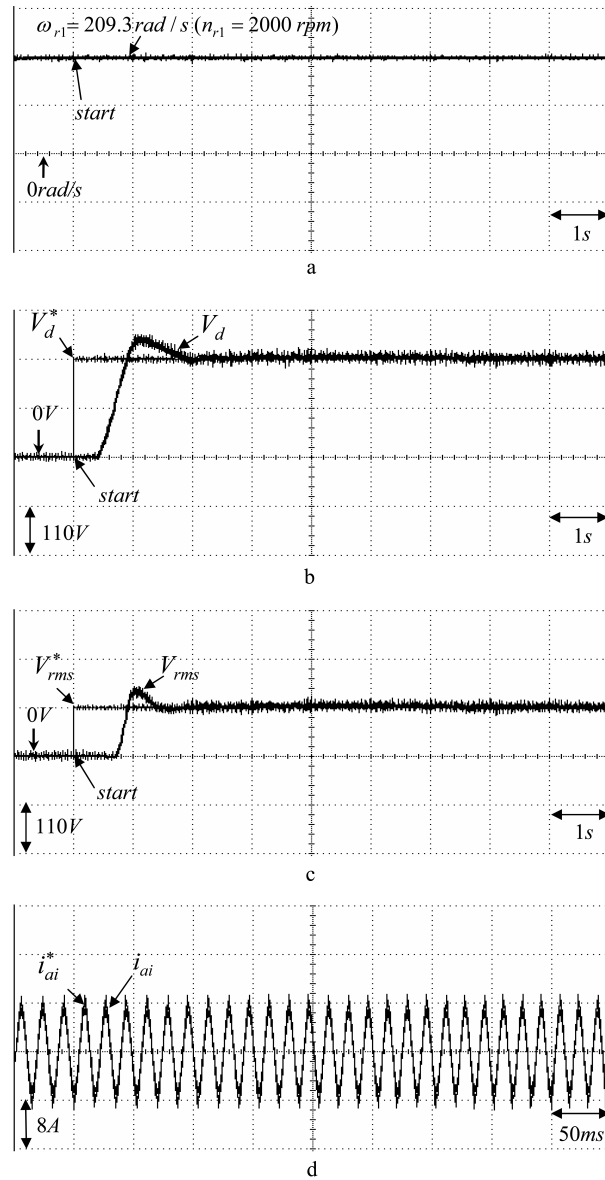

Figure 17. Experimental results of the PMSM direct-drive PMSG system using the second kind of recurrent wavelet NN controller for the Δ connection 3-phase loads of 18 Ω with ω_{r1} = 209.3 rad/s (n_{r1} = 2000 rpm) in case 3: a) rotor speed $\omega_{r1}(n_{r1})$; b) adjusting responses of the step desired magnitude V_d^* of the DC bus voltage and the actual measured magnitude V_d of the DC bus voltage in the output end of the rectifier; c) adjusting responses of the step desired root-mean-square magnitude V_{rms}^* of the AC 60-Hz line voltage and actual measured root-mean-square magnitude V_{rms} of the AC 60-Hz line voltage in the output end of the inverter V_{rms}; and d) tracking responses of the desired phase current i_{ai}^* and actual measured phase current i_{ai} in phase ai of the inverter.

the PI control method and the conventional NN control, the proposed recurrent wavelet NN control method improves the tracking ability and reduces the oscillations in steady-state.

5. Conclusions

This study demonstrates the implementation of both the DC bus voltage and AC 60-Hz line voltage adjustment of a PMSG system direct-driven by a PMSM based on a wind turbine emulator, using 2 sets of the same recurrent wavelet NN controllers for stand-alone power applications. First, the field-oriented control is implemented for the control of the PMSG system direct-driven by a PMSM based on a wind turbine emulator. Next, 2 sets of the same recurrent wavelet NN controllers are proposed to adjust the DC bus voltage of the rectifier and the AC 60-Hz line voltage of the inverter. In addition, the control performance of the proposed recurrent wavelet NN-controlled PMSM direct-drive PMSG system is robust with regard to the 2 operating conditions of the PMSG. Because of the weak robustness of the linear controller for the PI-controlled PMSM direct-drive PMSG system, dull DC bus voltage and AC 60-Hz line voltage adjusting responses are obviously obtained from the experimental results. The important contribution of this study is the successful application of the 2 sets of the same recurrent wavelet NN controllers on the PMSM direct-drive PMSG system to adjust the DC bus voltage of the rectifier and the AC 60-Hz line voltage of the inverter with robust control performance. Finally, the control performance of the proposed recurrent wavelet NN controller shown in the experimental results is superior to the PI controller and conventional NN controller for the PMSG system direct-driven by a PMSM based on a wind turbine emulator with a rectifier and an inverter for stand-alone power applications. The system of the proposed control scheme will extend to be applied for the grid system of electric utilities with battery energy storage due to the raised reliability of the system in the future.

Nomenclature

v_{d1}, v_{q1}	d and q axis stator voltages of the permanent magnet synchronous generator (PMSG)
i_{d1}, i_{q1}	d and q axis stator currents of the PMSG
L_{d1}, L_{q1}	d and q axis inductances of the PMSG
R_{s1}	Phase winding resistance of the PMSG
ω_{r1}, n_{r1}	Rotor angular velocity of the PMSG in rad/s, in rpm
λ_{pm}	Permanent magnet mutual flux linkage of the PMSG
P	Number of poles of the PMSG
β	Tip ratio of the wind turbine
R_1	Turbine rotor radius of the wind turbine
T_1	Output torque of the wind turbine
T_e	Electromagnetic torque of the PMSG
J_1	Moment of inertia of the PMSG
B_1	Viscous friction coefficient of the PMSG
ρ_1	Density of the air
K_t	Torque constant of the PMSG

A_1	Exposed area of the wind turbine
$H_p(s) = \frac{1}{Js+B} = \frac{b}{s+a}$	Coefficient of power performance
P_1	Output mechanical power of the wind turbine
v_1	Wind speed
θ_{r1}	Rotor position of the PMSG
θ_{i1}	Electric angular angle of the inverter
i_{dr}^*, i_{qr}^*	d and $q$axis control current of the rectifier
$i_{ar}^*, i_{br}^*, i_{cr}^*$	Desired phase currents of the PMSG in phases ar, br, and cr
i_{ar}, i_{br}, i_{cr}	Actual measured phase currents of the PMSG in phases ar, br, and cr
T_{ar}, T_{br}, T_{cr}	Sinusoidal pulse-width modulation (PWM) control signals of the rectifier in phases ar, br, and cr
V_d, V_d^*	Actual measured magnitude of the DC bus voltage of the rectifier, desired magnitude of the DC bus voltage of the rectifier
i_{di}^*, i_{qi}^*	d and $q$axis control current of the inverter
$i_{ai}^*, i_{bi}^*, i_{ci}^*$	Desired phase currents of the inverter in phases ai, bi, and ci
i_{ai}, i_{bi}, i_{ci}	Actual measured phase currents of the inverter in phases ai, bi, and ci
T_{ai}, T_{bi}, T_{ci}	Sinusoidal PWM control signals of the inverter in phases ai, bi, and ci
V_{rms}, V_{rms}^*	Actual measured root-mean-square magnitude of the AC 60-Hz line voltage of the inverter, desired root-mean-square magnitude of the AC 60-Hz line voltage of the inverter
$c_{i,m}^1, c_{i,m}^2, c_{j,m}^3, c_{k,m}^4$	Inputs of nodes in the input layer, mother wavelet layer, wavelet layer, and output layer of the mth recurrent wavelet neural network (NN)
$g_{i,m}^1, g_{j,m}^2, g_{k,m}^3, g_{o,m}^4$	Activation functions in the input layer, mother wavelet layer, wavelet layer, and output layer of the mth recurrent wavelet NN
$nod_{i,m}^1, nod_{j,m}^2, nod_{k,m}^3, nod_{o,m}^4$	Mode functions in the input layer, mother wavelet layer, wavelet layer, and output layer of the mth recurrent wavelet NN
$d_{i,m}^1, d_{j,m}^2, d_{k,m}^3, d_{o,m}^4$	Output of nodes in the input layer, mother wavelet layer, wavelet layer, and output layer of the mth recurrent wavelet NN
$\phi(x)$	Derivative of the Gaussian wavelet function in the mother wavelet layer
N	Number of iterations
l_1	Total number of wavelets
$a_{ij,m}, b_{ij,m}$	Translations and dilations of the mother wavelet layer in the mth recurrent wavelet NN
n	Total number of the mother wavelets
$\mu_{jk,m}^3$	Connective weights between the mother wavelet layer (j layer) and wavelet layer (k layer) in the mth recurrent wavelet NN
$\mu_{ko,m}^4$	Connective weights between the mother wavelet layer (k layer) and output layer (o layer) in the mth recurrent wavelet NN
$\mu_{oi,m}$	Recurrent weights between the output layer (o layer) and input layer (i layer) in the mth recurrent wavelet NN
$d_{o,1}^4 = U_{R\,1}, d_{o,2}^4 = U_{R\,2}$	Output of the output layer in the first recurrent wavelet NN, output of the output layer in the second recurrent wavelet NN
ψ_m	Collection vector of the adjustable parameters in$m$th recurrent wavelet NN
χ_m	Input vector of the output layer in the mth recurrent wavelet NN
γ	Learning rate
$\Delta a_{ij,m}, \Delta b_{ij,m}$	Variation of the translations and dilations in the mth recurrent wavelet NN
$\Delta \mu_{k,m}^3$	Variation of the connective weights in the mth recurrent wavelet NN
$\Delta \mu_{oi,m}$	Variation of the recurrent weights in the mth recurrent wavelet NN
$\upsilon_m^4, \upsilon_{k,\,m}^3, \upsilon_{j,m}^2$	Propagated error terms in the mth recurrent wavelet NN
$V_{c,m}$	Energy function in the mth recurrent wavelet NN

References

[1] K. Tan, S. Islam, "Optimum control strategies in energy conversion of PMSG wind turbine system without mechanical sensors", IEEE Transactions on Energy Conversion, Vol. 19, pp. 392–400, 2004.

[2] M. Kolhe, J.C. Joshi, D.P. Kothari, "Performance analysis of a directly coupled photovoltaic water-pumping system", IEEE Transactions on Energy Conversion, Vol. 19, pp. 613–618, 2004.

[3] G.K. Andersen, C. Klumpner, S.B. Kjaer, F. Blaabjerg, "A new green power inverter for fuel cells", Proceedings of the IEEE 33rd Annual Power Electronics Specialists Conference, pp. 727–733, 2002.

[4] Z. Lubosny, Wind Turbine Operation in Electric Power Systems, Berlin, Springer, 2003.

[5] T. Ackermann, Wind Power in Power Systems, New York, Wiley, 2005.

[6] M. Karrari, W. Rosehart, O.P. Malik, "Comprehensive control strategy for a variable speed cage machine wind generation unit", IEEE Transactions on Energy Conversion, Vol. 20, pp. 415–423, 2005.

[7] I. Boldea, Synchronous Generators, Boca Raton, FL, USA, Taylor and Francis, 2006.

[8] M. Chinchilla, S. Arnaltes, I.C. Burgos, "Control of permanent magnet generators applied to variable-speed wind-energy systems connected to the grid", IEEE Transactions on Energy Conversion, Vol. 21, pp. 130–135, 2006.

[9] S. Sajedi, F. Kahlifeh, T. Karimi, Z. Khalifeh, "Maximum power point tracking of variable speed wind energy conversion system", International Journal of Physical Sciences, Vol. 6, pp. 6843–6851, 2011.

[10] F. Gharedaghi, H. Jamali, M. Deysi, A Khalili, "Maximum power point tracking of variable speed wind generation system connected to permanent magnet synchronous generator", International Review of Electrical Engineering, Vol. 4, pp. 1044–1049, 2011.

[11] B. Delyon, A. Juditsky, A. Benveniste, "Accuracy analysis for wavelet approximations", IEEE Transactions on Neural Networks, Vol. 6, pp. 332–348, 1995.

[12] C.F. Chen, C.H. Hsiao, "Wavelet approach to optimizing dynamic systems", IEE Proceedings – Control Theory and Applications, Vol. 146, pp. 213–219, 1999.

[13] Q. Zhang, A. Benveniste, "Wavelet networks", IEEE Transactions on Neural Networks, Vol. 3, pp. 889–898, 1992.

[14] J. Zhang, G.G. Walter, Y. Miao, W.N.W. Lee, "Wavelet neural networks for function learning", IEEE Transactions on Signal Processing, Vol. 43, pp. 1485–1496, 1995.

[15] Z. Zhang, C. Zhao, "A fast learning algorithm for wavelet network and its application in control", Proceedings of IEEE International Conference on Control Automation, pp. 1403–1407, 2007.

[16] H.L. Wei, S.A. Billings, "A unified wavelet-based modelling framework for nonlinear system identification: the WANARX model structure", International Journal of Control, Vol. 77, pp. 351–366, 2004.

[17] H.L. Wei, S.A. Billings, M.A. Balikhin, "Wavelet based nonparametric NARX models for nonlinear input-output system identification", International Journal of Systems Science, Vol. 37, pp. 1089–1096, 2006.

[18] M. Ravan, R.K. Amineh, M. Karrari, W.B. Rosehart, O.P. Malik, "Synchronous machine model identification using continuous wavelet NARX network", Proceedings of the Institution of Mechanical Engineers – Part I: Journal of Systems and Control Engineering, Vol. 223, pp. 467–477, 2009.

[19] J. Xu, D.W.C. Ho, D. Zhou, "Adaptive wavelet networks for nonlinear system identification", Proceedings of the American Control Conference, pp. 3472–3473, 1997.

[20] N. Sureshbabu, J.A. Farrell, "Wavelet-based system identification for nonlinear control", IEEE Transactions on Automatic Control, Vol. 44, pp. 412–417, 1999.

[21] S.A. Billings, H.L. Wei, "A new class of wavelet networks for nonlinear system identification", IEEE Transactions on Neural Networks, Vol. 16, pp. 862–874, 2005.

[22] R.H. Abiyev, O.Kaynak, "Fuzzy wavelet neural networks for identification and control of dynamic plants—a novel structure and a comparative study", IEEE Transactions on Industrial Electronics, Vol. 55, pp. 3133–3140, 2008.

[23] D. Giaouris, J.W. Finch, O.C. Ferreira, R.M. Kennel, G.M. El-Murr, "Wavelet denoising for electric drives", IEEE Transactions on Industrial Electronics, Vol. 55, pp. 543–550, 2008.

[24] D. Gonzalez, J.T. Bialasiewicz, J. Balcells, J. Gago, "Wavelet-based performance evaluation of power converters operating with modulated switching frequency", IEEE Transactions on Industrial Electronics, Vol. 55, pp. 3167–3176, 2008.

[25] F.J. Lin, R.J. Wai, M.P. Chen, "Wavelet neural network control for linear ultrasonic motor drive via adaptive sliding-mode technique", IEEE Transactions on Ultrasonics, Ferroelectrics, and Frequency Control, Vol. 50, pp. 686–697, 2003.

[26] G. Gokmen, "Wavelet based instantaneous reactive power calculation method and a power system application sample", International Review of Electrical Engineering, Vol. 4, pp. 745–752, 2011.

[27] S.H. Ling, H.H.C. Iu, F.H.F. Leung, K.Y. Chan, "Improved hybrid particle swarm optimized wavelet neural network for modeling the development of fluid dispensing for electronic packaging", IEEE Transactions on Industrial Electronics, Vol. 55, pp. 3447–3460, 2008.

[28] S. Partal, İ. Şenol, A.F. Bakan, K.N. Bekiroğlu, "Online speed control of a brushless AC servomotor based on artificial neural networks", Turkish Journal of Electrical Engineering & Computer Sciences, Vol. 19, pp. 373–383, 2011.

[29] A.T. Özdemir, K. Danışman, "Fully parallel ANN-based arrhythmia classifier on a single-chip FPGA: FPAAC", Turkish Journal of Electrical Engineering & Computer Sciences, Vol. 19, pp. 667–687, 2011.

[30] A.A. Kulaksız, R. Akkaya, "Training data optimization for ANNs using genetic algorithms to enhance MPPT efficiency of a stand-alone PV system", Turkish Journal of Electrical Engineering & Computer Sciences, Vol. 20, pp. 241–254, 2012.

[31] M. Moazzami, R.A. Hooshmand, "Short-term nodal congestion price forecasting in a large-scale power market using ANN with genetic optimization training", Turkish Journal of Electrical Engineering & Computer Sciences, Vol. 20, pp. 751–768, 2012.

[32] H. Bouzari, H. Moradi, E. Bouzari, "Adaptive neuro-wavelet system for the robust control of switching power supplies", IEEE International Multitopic Conference, pp. 1–6, 2008.

[33] K. Funahashi, Y. Nakamura, "Approximation of dynamical systems by continuous time recurrent neural network", Neural Networks, Vol. 6, pp. 801–806, 1993.

[34] L. Jin, P.N. Nikiforuk, M. Gupta, "Approximation of discrete-time state-space trajectories using dynamic recurrent networks", IEEE Transactions on Automatic Control, Vol. 6. pp. 1266–1270, 1995.

[35] C.C. Ku, K.Y. Lee, "Diagonal recurrent neural networks for dynamical system control", IEEE Transactions on Neural Networks, Vol. 6, pp. 144–156, 1995.

[36] C.H. Lu, C.C. Tsai, "Adaptive predictive control with recurrent neural network for industrial processes: an application to temperature control of a variable-frequency oil-cooling machine", IEEE Transactions on Industrial Electronics, Vol. 55, pp. 1366–1375, 2008.

[37] P. Brandstetter, M. Kuchar, I. Neborak, "Selected applications of artificial neural networks in the control of AC induction motor drives", International Review of Electrical Engineering, Vol. 4, pp. 1084–1093, 2011.

[38] M. Ghariani, I.B. Salah, M. Ayadi, R. Neji, "Neural induction machine observer for electric vehicle applications", International Review of Electrical Engineering, Vol. 3, pp. 314–324, 2010.

[39] S.J. Yoo, J.B. Park, Y.H. Choi, "Stable predictive control of chaotic systems using self-recurrent wavelet neural network", International Journal of Automatic Control Systems, Vol. 3, pp. 43–55, 2005.

[40] S.J. Yoo, Y.H. Choi, J.B. Park, "Generalized predictive control based on self-recurrent wavelet neural network for stable path tracking of mobile robots: adaptive learning rates approach", IEEE Transactions on Circuits and Systems I, Vol. 53, pp. 1381–1394, 2006.

[41] C.H. Lu, "Design and application of stable predictive controller using recurrent wavelet neural networks", IEEE Transactions on Industrial Electronics, Vol. 56, pp. 3733–3742, 2009.

[42] C.H. Chen, C.F. Hsu, "Recurrent wavelet neural backstepping controller design with a smooth compensator", Neural Computation and Applications, Vol. 19, pp. 1089–1100, 2010.

[43] S.I. Han, J.M. Lee, "Adaptive dynamic surface control with sliding mode control and RWNN for robust positioning of a linear motion stage", Mechatronics, Vol. 22, pp. 222–238, 2012.

[44] F.J. Lin, L.T. Teng, M.H. Yu, "Radial basis function network control with improved particle swarm optimization for induction generator system", IEEE Transactions on Power Electronics, Vol. 23, pp. 2157–2169, 2008.

[45] Y. Oussar, G. Dreyfus, "Initialization by selection for wavelet network training", Neurocomputing, Vol. 34, pp. 131–143, 2000.